Synthesis and Photophysical Behavior of Cu(I) Coordination Compounds

M.Sc. Thesis

By

AROSMIT MOHANTY

(2403131006)



DEPARTMENT OF CHEMISTRY

INDIAN INSTITUTE OF TECHNOLOGY INDORE

MAY 2026

Synthesis and Photophysical Behavior of Cu(I) Coordination Compounds

A THESIS

Submitted in partial fulfillment of the requirements for the award of the degree

of

Master of Science

by

Arosmit Mohanty

(2403131006)



DEPARTMENT OF CHEMISTRY

INDIAN INSTITUTE OF TECHNOLOGY INDORE

MAY 2026

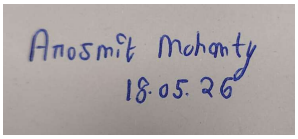
INDIAN INSTITUTE OF TECHNOLOGY

INDORE

CANDIDATE'S DECLARATION

I hereby certify that the work being presented in the thesis entitled **"Synthesis and Photophysical Behavior of Cu(I) Coordination Compounds"** in the partial fulfillment of the requirements for the award of the degree of **MASTER OF SCIENCE** and submitted to the **Department of Chemistry, Indian Institute of Technology Indore**, is an authentic record of my work carried out during the period from July 2025 to May 2026 under the supervision of **Dr. Abhinav Raghuvanshi**, Assistant Professor, Department of Chemistry, IIT Indore.

The matter presented in this thesis has not been submitted by me for the award of any other degree of this or any other institute.



Arosmit Mohanty

This is to certify that the above statement made by the candidate is correct to the best of my/our knowledge.



Dr. Abhinav Raghuvanshi

Arosmit Mohanty has successfully completed his M.Sc. Oral Examination held on **11/05/2026**.

ACKNOWLEDGEMENTS

First, I would like to express my deepest gratitude to my thesis supervisor, **Dr. Abhinav Raghuvanshi**, for providing me with guidance, supervision, and advice, and for consistently directing and guiding me toward the completion of my thesis. I am obliged to thank my mentor and all the seniors, **Mr. Anrudh Mishra**, **Mr. Sarvesh Maurya**, **Ms. Jyoti, Mr. Deepak**, **Ms. Prachi Singh** and **Mr. Vishal Kumar**; you all have constantly guided me and helped me during my lab work, despite having their own projects then have also given me suggestions that made this work possible. I would also like to thank my friends and family, who have constantly supported me, even during my times of failure.

Arosmit Mohanty

2403131006

MSc. Second Year

Department of Chemistry

Indian Institute of Technology Indore, India

DEDICATE TO MY FAMILY…….

ABSTRACT

Emissive materials have emerged as a key component in modern optoelectronic devices due to their tunable properties and ease of integration into device fabrication and modification. Here we report a series of four new Cu(I) complexes. These are synthesized using Cu(I) halides (I, Br, and Cl) as the metal source and a combination of ligands **PyCbz** and PPh_3. SCXRD analysis indicates that the complexes crystallize as dimeric Cu_2X_2 rhombic cores with symmetric ligand coordination. The structure and bulk-phase purity were confirmed by multinuclear NMR and PXRD analysis, respectively. **C1** exhibits a shorter Cu···Cu separation (2.625 Å), indicating moderate cuprophilic interaction. Further, under photoexcitation, **C1** shows a broadband visible-range emission with 61% PLQY. The temperature-dependent photoluminescence study shows a blueshift in the emission maxima with a minimal change in decay time with the lowering of temperature. This indicates the dominant role of phosphorescence in the emission mechanism, which is further supported by DFT studies. Additionally, the photophysical studies of complexes reveal intense visible-region emission with high PLQY, reaching 90% for **C2**. Among **C2**-**C4**, the emission maxima are tuned by substituting halide ions in the Cu_2X_2 unit. DFT calculations are used to determine the FMOs and elucidate charge transfer via the (M+X)LCT mechanism. The ΔE_{ST} is less than the typical upper limit (0.3 eV), indicating the presence of TADF at room temperature and phosphorescence at low temperature. This change in emission mechanism is further supported by a TDPL study of **C2**. Additionally, **C2** exhibits AIE, as evidenced by a significant enhancement in emission intensity in the aggregated state compared to the solution state. Furthermore, owing to **C2**'s excellent photoluminescent properties, a hybrid PPMA film was fabricated, retaining the complex's emissive efficiency and paving the way for potential optoelectronic applications.

TABLE OF CONTENT

LIST OF FIGURES	xiii
LIST OF SCHEMES	xvi
LIST OF TABLES	xvii
NOMENCLATURE	xviii
ACRONYMS	xix
Chapter 1: INTRODUCTION	1
1.1 Photoluminescent Materials	1
1.2 Copper(I) Complexes and the Effect of Halide Substitution	2
1.3 Carbazole-based Emitters	5
1.4 Aggregation-Induced Emission	6
Chapter 2: EXPERIMENTAL SECTION	8
2.1 Material and Instrumentation	8
2.2 Synthesis of Ligand	9
2.2.1 Synthesis of 9-(pyridine-4-yl)-9H-Carbazole	9
2.3 Synthesis of Complexes	10
2.3.1 Synthesis of **C1**	10
2.3.2 Synthesis of **C2**	10
2.3.3 Synthesis of **C3**	11
2.3.4 Synthesis of **C4**	12
Chapter 3: RESULTS AND DISCUSSION	13
3.1 Characterization	13
3.1.1 Characterization of Ligand	13
3.1.1.1 Characterization of **PyCbz**	13
3.1.2 Characterization of the Complexes	14
3.1.2.1 Characterization of **C1**	14
3.1.2.2 Characterization of **C2**	16
3.1.2.3 Characterization of **C3**	20

3.1.2.4 Characterization of **C4**	23
3.2 Photophysical Study	26
3.2.1 Solid State absorption Studies	26
3.2.2 Photoluminescent Study of **C1**-**C4**	27
3.3 Aggregation-Induced Emission behavior of **C2**	35
3.4 Film fabrication of **C1** and the corresponding photophysical study	37
Chapter 4: CONCLUSIONS AND FUTURE SCOPE	38
4.1 Conclusions	38
4.2 Future Scope	39
5. References	42

LIST OF FIGURES

Figure 1. Pictorial representation of various fields of application of photoluminescent materials. 1

Figure 2. Representative molecular structures of emissive transition-metal complexes. 2

Figure 3. Schematic representation of the pseudo-Jahn–Teller flattening distortion upon excitation in the MLCT excited state, leading to an increased accessibility of the copper center to nucleophiles (Nu). 3

Figure 4. (a) Phosphine-based complexes showing good luminescence efficiency. **(b)** Structures of di-nuclear Cu(I) halide-based complexes and **(c)** their photoluminescence spectra, illustrating halide-induced emission tuning. 4

Figure 5. (a) Phosphine-based complexes showing good luminescence efficiency. **(b)** Structures of di-nuclear Cu(I) halide-based complexes and **(c)** their photoluminescence spectra, illustrating halide-induced emission tuning. 5

Figure 6. (a) Schematic diagram of the synthesized cluster. **(**b-c**)** The photographic images of the aggregated mixtures prepared using DMSO and Water, from varying water content (f_{water}% = 30-90%). **(**d-e**)** The corresponding photoluminescence spectrum. 7
Figure 7. ^{1}H NMR of **PyCbz**. 13
Figure 8. $^{13}C\{^{1}H\}$ NMR of **PyCbz**. 14
Figure 9. Single crystal structure of **C1** (H-atoms are omitted for clarity). 15
Figure 10. Structural representations of complexes **C1** exhibiting the Cu···Cu distances (Å). 15
Figure 11. Comparison of the experimental and simulated PXRD patterns of the **C1**. 16
Figure 13. $^{13}C\{^{1}H\}$ NMR of **C2**. 18
Figure 14. $^{31}P\{^{1}H\}$ NMR of **C2**. 18
Figure 15. Structural representations of complexes **C2** exhibiting the Cu···Cu distances (Å). 19
Figure 16. Comparison of the experimental and simulated PXRD patterns of the **C2**. 19
Figure 17. ^{1}H NMR of **C3**. 20
Figure 18. $^{13}C\{^{1}H\}$ NMR of **C3**. 21
Figure 19. $^{31}P\{^{1}H\}$ NMR of **C3**. 21
Figure 20. Structural representations of complexes **C3** exhibiting the Cu···Cu distances (Å). 22
Figure 21. Comparison of the experimental and simulated PXRD patterns of the **C3**. 22
Figure 22. ^{1}H NMR of **C4**. 23

Figure 23. $^{13}C\{^{1}H\}$ NMR of **C4**. 24
Figure 24. $^{31}P\{^{1}H\}$ NMR of **C4**. 24
Figure 25. Structural representations of complexes **C4** exhibiting the Cu···Cu distances (Å). 25
Figure 26. Comparison of the experimental and simulated PXRD patterns of the **C4**. 25
Figure 27. UV-Vis DRS of **PyCbz** and **C1**-**C4**. 26
Figure 28 Solid-state PL spectrum of **C1**-**C2** recorded at room temperature. 27
Figure 29. (a) TDPL spectrum of **C1** recorded between 10-300 K (On photoexcitation at 345 nm). **(b)** Temperature-dependent lifetime plots of **C1**. **(c)** Lifetime vs temperature plot for **C1**. **(d)** TDPL spectrum of **C2** recorded between 10-300 K (On photoexcitation at 365 nm). **(e)** Temperature-dependent lifetime plots of **C2**. **(f)** Lifetime vs temperature plot with Boltzmann-type fitting for **C2**. **(g)** Energy-level diagrams representing the excitation-emission mechanism of **C1** at both room temperature and low temperatures. **(h & i)** Energy-level diagrams representing the excitation-emission mechanism of **C2** at room temperature and low temperature, respectively. 31
Figure 30. Solid-state photoluminescence spectrum of **(a) C3** and **(b) C4** at r.t. and 77K. 35

Figure 31. (a) The photographs of aggregated mixtures of **C2**, under UV light (λ= 365 nm), with the order of increasing f_w%. **(b)** The corresponding photoluminescence spectra with λ_{ex}= 365 nm. **(c)** DLS of an aggregated mixture of **C2** at f_w= 90%.. 36

Figure 32. Comparison of the solid-state photoluminescent spectrum of the fabricated **C2** film and its solid powder. 37

LIST OF SCHEMES

Scheme 1. Synthesis of **PyCbz**. 9

Scheme 2. Synthesis of **C1**. 10

Scheme 3. Synthesis of **C2**. 11

Scheme 4. Synthesis of **C3**. 11

Scheme 5. Synthesis of **C4**. 12

LIST OF TABLES

Table 1. The summery the photophysical properties of **C1**-**C4**. 28

Table 2. DFT calculated geometry-optimized structure and frontier molecular orbitals for **C1**-**C4**. 28

Table 3. TDPL and temperature-dependent decay times of **C1**. 30

Table 4. TDPL and temperature-dependent decay times of **C2**. 32

NOMENCLATURE

π	pi
δ	Chemical shift
μm	Micrometer
nm	Nanometer
K	Kelvin
mmol	Milimole
mL	MiliLiters
r.t.	Room temperature
ΔE_{ST}	Singlet-triplet energy gap
kB	Boltzmann Constant

ACRONYMS

$CDCl_3$	Chloroform-d
TMS	Tetramethyl Silane
MeCN	Acetonitrile
MeOH	Methanol
EA	Ethylacetate
DMSO	Dimethyl Sulphoxide
DCM	Dichloromethane
HRMS	High-resolution Mass Spectrometry
NMR	Nuclear Magnetic Resonance
UV-Vis	Ultraviolet-Visible
PyCbz	9-(pyridine-4-yl)-9H-Carbazole
TADF	Thermally-activated delayed fluorescence
TDPL	Temperature-dependent photoluminescence
UV-Vis DRS	Ultraviolet-Visible Diffuse Reflectance Spectroscopy
PL	Photo-Luminescence
PLQY	Photo-Luminescent Quantum Yield
DFT	Density Functional Theory
TD-DFT	Time-Dependent Density Functional Theory
FMO	Frontier Molecular Orbital
HOMO	Highest Occupied Molecular Orbital
LUMO	Lowest Unoccupied Molecular Orbital
DLS	Dynamic Light Scattering
FWHM	Full Width Half Maxima
OLED	Organic light-emitting diode
LEEC	Light-emitting electrolytic cell
SOC	Spin-orbit coupling

Chapter 1: INTRODUCTION

1.1 Photoluminescent Materials:

Photoluminescent materials, consisting of organic fluorophores, metal complexes, and polymers**,** have the property of excellent light absorption and efficient conversion to light, energy, etc.*[1,2]* This enables their diverse applications in optoelectronics, such as organic light-emitting diodes (OLEDs), light-emitting electrolytic cells (LEECs), and dye-sensitized solar cells, as well as in photocatalysis, chemical and electrochemical sensors, and bioimaging materials (Figure 1).*[3-6]*

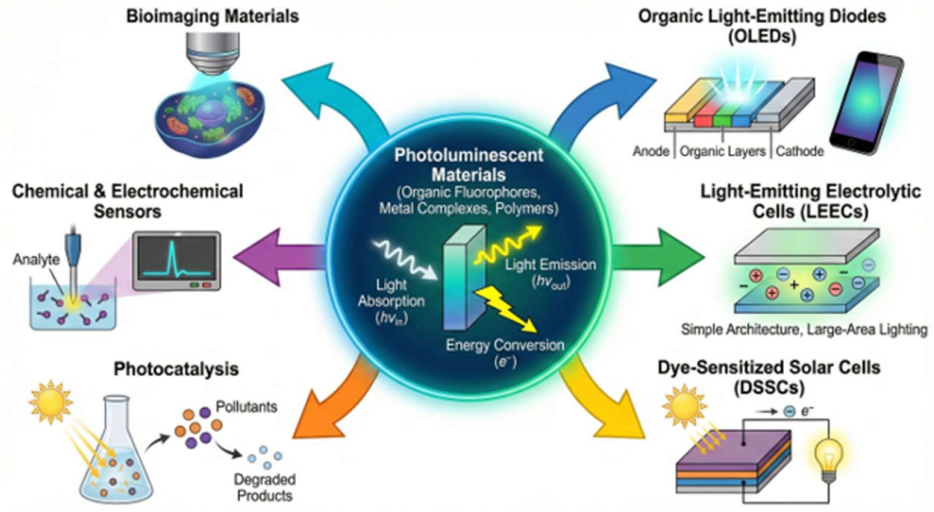


Figure 1. Pictorial representation of various fields of application of photoluminescent materials. *[7]*

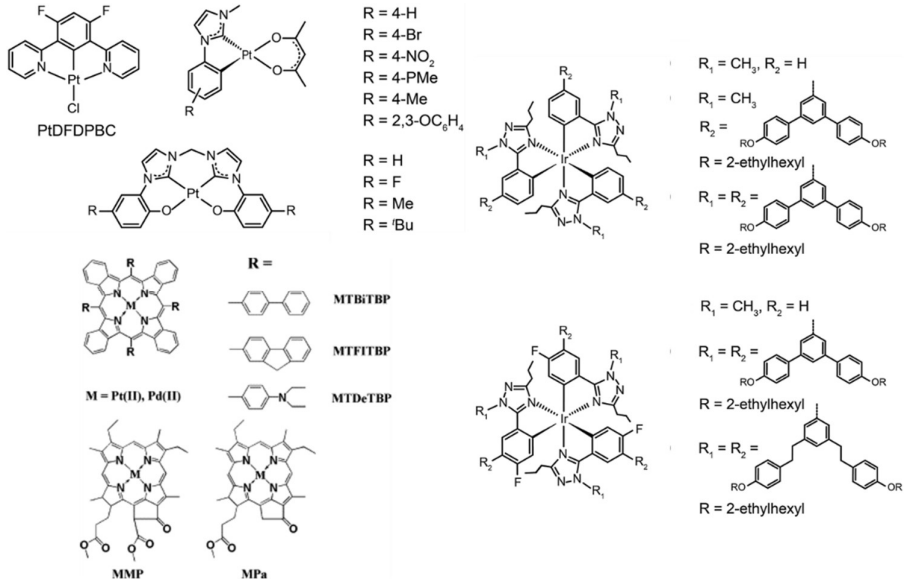


Figure 2. Representative molecular structures of emissive transition-metal complexes. *[8-10]*

For the manufacturing of these materials, various metal complexes are widely used, particularly those based on iridium, platinum, and palladium (Figure 2). Due to their large nuclear charge, these metals exhibit exceptionally strong SOC, leading to intense emission with a high PLQY.*[8-10]* Although those metal complexes exhibit excellent emission characteristics, the structural instability of the organometallic compounds, the high cost of metal source, and the inherent toxicity associated with the material processing make them unfavorable for practical application.*[11,12]* These problems can be overcome by replacing heavy metals with copper.

1.2 Copper(I) Complexes and the Effect of Halide Substitution:

Copper is an earth-abundant, cost-effective material that offers a promising alternative to rare-earth elements.*[13-15]* Cu(I) in particular exhibits a diverse range of coordination environments, including tetrahedral, trigonal planar, and linear. Unlike Pt, Pd, and Ir complexes, Cu(I) complexes benefit from a fully filled d-orbital, which prevents ground-state Jahn-Teller Distortion (JTD) and marks a greater structural stability. *[16]* But the lower SOC of copper than

that of rare-earth elements hinders its application as an emitter material. This can be compensated for by introducing halides into the copper(I) coordination environment. Halogen atoms, due to their bulkier sizes, enhance radiative rates by supporting greater SOC. *[17,18]* Further, the presence of bridging halogens provides greater structural stability, thereby enhancing the durability of the complexes. *[19]*

The d^{10} electronic system of Cu(I) prevents JTD, and the resulting complex is structurally stable in the ground state. But in the excited state, Cu(I) is converted to a d^9 system, and, due to an asymmetric arrangement, it undergoes a distortion termed the pseudo-Jahn-Teller distortion (pseudo-JTD) (Figure 3). *[17]*

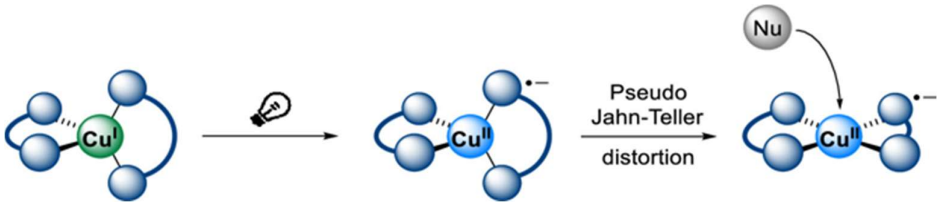


Figure 3. Schematic representation of the pseudo (Nu = Nucleophile) (Taken from reference number 17).

For prevention, bulky phosphine-based ligands are widely used, providing steric protection against the distortion. Additionally, the strong sigma-donating nature of phosphine, along with the soft-soft interaction between Cu and P, facilitates the enhancement of MLCT transitions and results in efficient emission. *[20,21]* Paukar et. al. has reported homoleptic $[Cu(N\hat{}N)_2]^+$ and heteroleptic $[Cu(N\hat{}N)(P\hat{}P)]^+$ systems. Due to pronounced excited-state flattening, homoleptic complexes exhibited low PLQY. Further, the introduction of phosphines works in the reduction of flattening and increases luminescence (Figure 4a). *[22]*

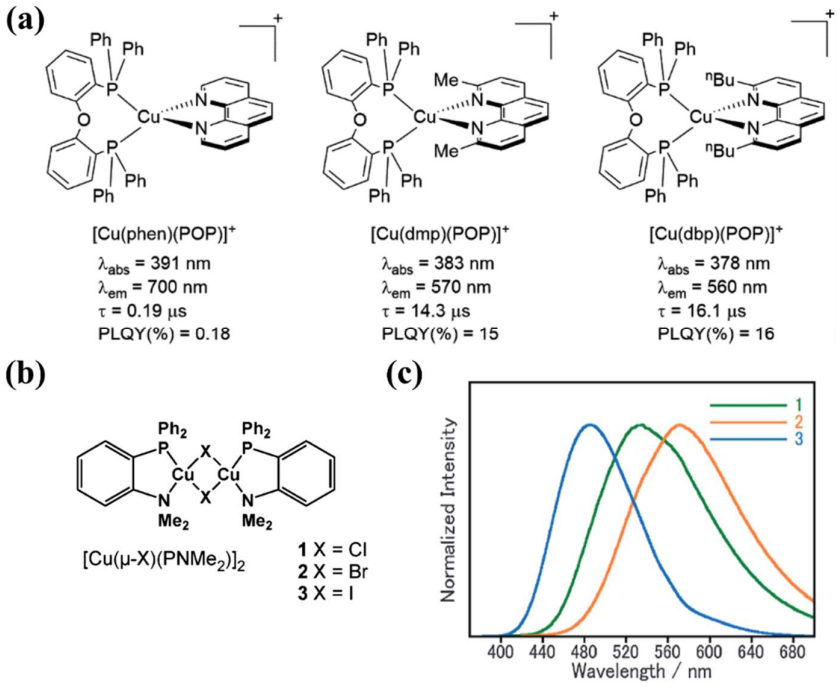


Figure 4. (a) Phosphine-based complexes showing good luminescence efficiency (Taken from reference number 22). **(b)** Structures of di-nuclear Cu(I) halide-based complexes and **(c)** their photoluminescence spectra, illustrating halide-induced emission tuning (Taken from reference number 19).

The emission wavelength is highly sensitive to factors such as ligand-field strength, charge-transfer direction, transfer efficiency, molecular rigidity, and intermolecular interactions. As a result, achieving facile, predictable tuning of emission wavelength in luminescent materials remains a challenge due to the intricate interplay among electronic structure, coordination environment, and solid-state effects. Additionally, the strategy of ligand modification often involves multistep synthesis and unpredictable changes in the emissive states. As a solution, halide substitution offers a straightforward and comprehensive approach to emission tuning. Variation in halide ions (I^-, Br^-, & Cl^-) modulates the ligand-field strength, polarizability, and the SOC, thereby influencing the luminescence wavelength and the corresponding efficiency. In this

context, Leitl et al. described a blue-and green-luminescent Cu(I) dimer that exhibits efficient singlet harvesting. Here, the author synthesized three complexes by varying the halides and observed a corresponding blue shift in the emission maxima with decreasing ligand-field strength (Cl^-> Br^-> I^-), highlighting the ease of tuning the emission (Figure 4b & c). *[19]*

1.3 Carbazole-based Emitters:

Carbazole has emerged as a highly versatile moiety in photoluminescent materials due to its extended electronic conjugation and structural rigidity. This unique property makes the carbazole moiety useful across a wide range of fields, including as an organic emitter, in an inorganic coordination system, and as a host in hybrid materials (Figure 5). In purely organic emitters, carbazole functions primarily as a strong electron-donating unit within the donor-acceptor system. The extended conjugated system enables efficient intramolecular charge transfer and facilitates excellent photoluminescence.

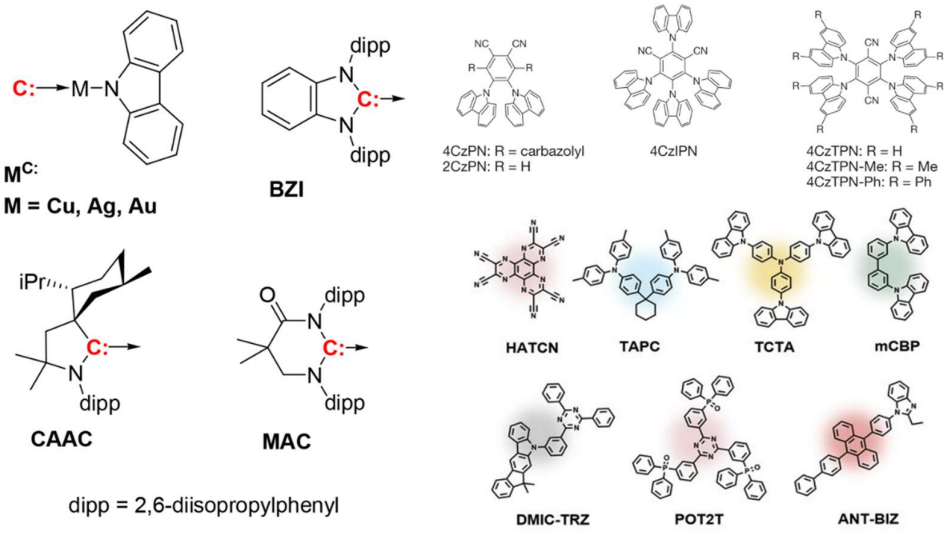


Figure 5. Overview of carbazole-based metal complexes and representative organic functional materials used in optoelectronic applications (Taken from reference numbers 23-25).

Hiroki et al. have designed 4CzIPN, a carbazole-embedded system. *[23]* The spatial separation of frontier molecular orbitals and the small singlet-triplet energy gap have enabled efficient harvesting of both singlet and triplet electrons, yielding a high PLQY of ≈ 94%. Further, in inorganic metal complexes, Hamze et al. and Muniz et al. separately reported a set of coinage-metal-based coordination complexes, in which the use of carbazole has led to efficient charge-transfer and long-lived excited states with high photoluminescence efficiency. *[24]* For the application of functional materials in optoelectronics, the emissive materials must be fabricated as films. In this context, various carbazole-based hosts are being used, which are known to provide structural stability and enhanced charge transfer, thereby leading to an efficient luminescent material. This is evidenced in an amide-carbene system (Cu-DBC), where the use of 1,3-dihydro-1,1-dimethyl-3-(3(4,6-diphenyl-1,3,5-triazin-2-yl)phenyl)indeno-[2,1b]carbazole (DMIC-TRZ) and 1,3-bis(N-carbazolyl)benzene (mCBP) has increased the emission efficacy. *[25]*

1.4 Aggregation-Induced Emission (AIE):

The emission behavior of the luminescent compounds is strongly influenced by crystal packing and their local coordination environments. In this context, various coordination systems have been reported to exhibit aggregation-induced emission (AIE), in which species that are weakly to non-emissive in solution become highly luminescent upon aggregation. *[26,27]* This occurs because intra- or intermolecular motions are hindered, reducing non-radiative decay and enhancing radiative emission. *[28]* This property enables applications in chemical and biological sensing, where the material acts as a "turn-on" fluorescent device for the sensing of metal ions and biomolecules with high sensitivity and selectivity. *[29-31]* In this context, Utrera-Melero *et al.* studied cubane-type copper(I) iodide clusters of the general formula $[Cu_4I_4L_4]$ (L=$PPh_3(C_6H_4\text{-}CH_2OH)$ and $PPh_2(C_3H_7)$), coordinated by phosphine ligands. *[32]* These

complexes display pronounced AIE, showing weak luminescence in solution but strong emission upon aggregation. In the aggregated state, due to close packing, the intramolecular motions are restricted. This reduces non-radiative transitions and enhances luminescent properties (Figure 6).

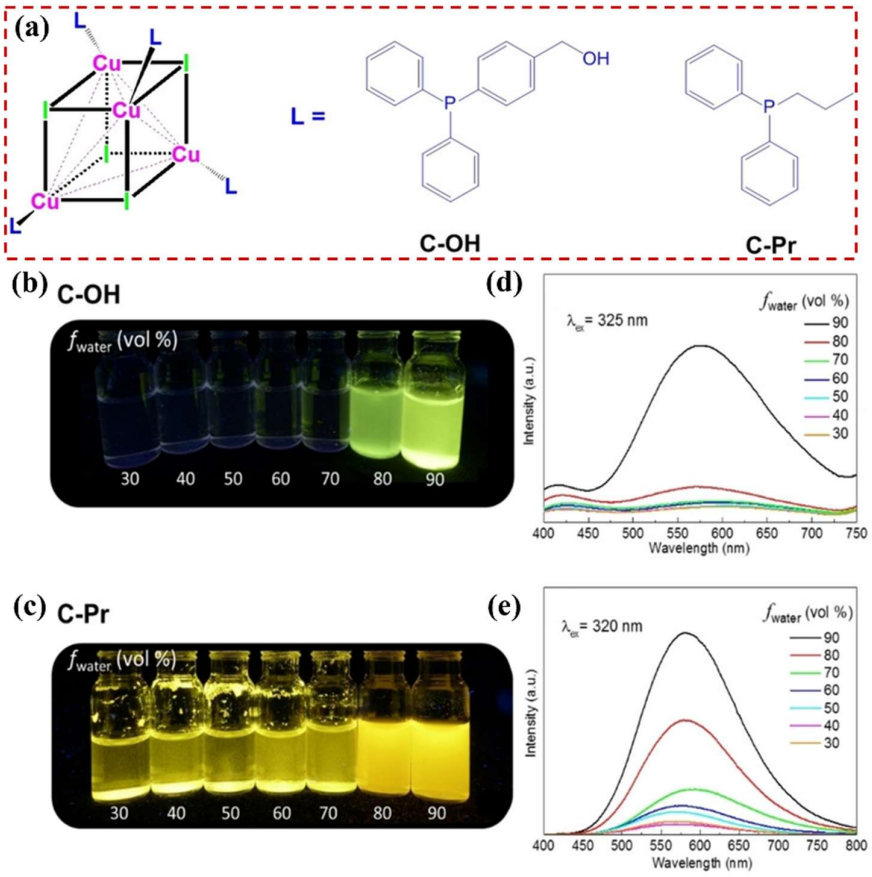


Figure 6. (a) Schematic diagram of the synthesized cluster. **(b-c)** The photographic images of the aggregated mixtures prepared using DMSO and Water, from varying water content (f_{water}% = 30-90%). **(d-e)** The corresponding photoluminescence spectrum (Taken from reference number 32).

Chapter 2: EXPERIMENTAL SECTION

2.1 Materials and Instrumentation:

Unless otherwise specified, chemicals were used exactly as received. TLC was used to monitor reaction progress on a Merck 60 F254 precoated silica gel plate (0.25 mm thickness), and the products were visualized under UV light. The Liquid Chromatography-High-Resolution Mass Spectrometry (LC-HRMS) instrument includes an ACQUITY H-Class Plus UPLC coupled to an Xevo G3 QTOF Mass Spectrometer. All ^{1}H and $^{13}C\{^{1}H\}$ and $^{31}P\{^{1}H\}$ NMR spectra were collected using a Bruker 400/500 spectrometer in $CDCl_3$. Data for proton NMR chemical shifts are shown in ppm downfield from TMS and are mentioned in delta (δ) units. $CDCl_3$ is used as an internal standard, which shows a peak at 7.26 ppm (^{1}H NMR) and 77.16 ppm ($^{13}C\{^{1}H\}$ NMR). The ^{1}H NMR splitting patterns are singlet (s), doublet (d), triplet (t), and multiplet (m), and the NMR data were processed using MestreNova. Rigaku Smart X-ray diffractometer with monochromatic Cu Kα (0.1540 nm) radiation in a 2θ range of 5-50 degrees was utilized to assess the phase purity of the complexes. The complexes are further characterized by single-crystal X-ray diffraction using a dual-source SuperNova CCD (Agilent Technologies, Oxford Diffraction) with Mo-Kα radiation (λ = 0.71073 Å) at 293 K. The structure solution was performed in OLEX2 with the SHELXT structure solution program using Intrinsic Phasing, and the structure was refined with SHELXL using least-squares. The UV-Vis DRS experiment is performed on a Shimadzu 2300i over the range of 300-1400 nm using Barium sulfate as a reference. A FLS1000 spectrometer from Edinburgh Instruments was used to record the luminescence spectra of all compounds at an excitation wavelength of 340-370 nm. OriginPro 2026 was used to plot each luminescence emission spectrum. DLS and Zeta potential experiments were performed at ambient temperature on a NanoPlus 3 (Micromeritics) instrument. DFT and TD-DFT calculations were

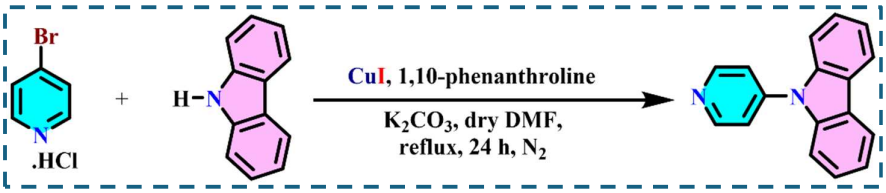
performed using the Gaussian 09 program and MobaXterm. DFT calculations at the B3LYP/6-31G* level were used to optimize the ground-state geometries of the investigated compounds, and the associated basis sets were LANL2DZ for Cu and the halides (I, Br, and Cl). TD-DFT calculations were performed at the same level of theory using the optimized ground-state geometries. The distribution of FMOs and their associated energies was visualized using GaussView. The singlet and triplet excited-state (S_1/T_1) geometries of the complexes were optimized at the TD-B3LYP/LAN2DZ level using the respective ground-state geometries. The corresponding energies are also calculated.

2.2 Synthesis of Ligand:

2.2.1 Synthesis of 9-(pyridine-4-yl)-9H-Carbazole:

The ligand 9-(pyridine-4-yl)-9H-Carbazole (**PyCbz**) was prepared by following a literature procedure. *[33]* In a clean and oven-dried two-neck round-bottom flask, carbazole (167.2 mg, 1.0 mmol, 1.0 equiv), 4-bromopyridine·HCl (252.8 mg, 1.3 mmol, 1.3 equiv), copper(I) iodide (30.5 mg, 0.16 mmol, 0.16 equiv), 1,10-phenanthroline (63.4 mg, 0.32 mmol, 0.32 equiv), and potassium carbonate (552.8 mg, 4.0 mmol, 4.0 equiv) were added to dry N, N-dimethylformamide (DMF) (8 mL). The reaction is refluxed with continuous stirring for 24 h under an inert nitrogen condition. After completion of the reaction, the mixture was cooled to room temperature, and then the solvent was removed under reduced pressure. The resulting residue was subjected to an aqueous workup involving extraction by DCM and a cold brine solution. The organic layer was collected, dried with anhydrous sodium sulfate, filtered, and concentrated under vacuum to yield the crude product. Purification of the crude material was carried out by column chromatography on silica gel using a 5:95 (v/v %) EA/hexane eluent. The ligand was obtained as an off-white solid with 85% yield. **^{1}H NMR (500 MHz, $CDCl_3$)** δ 8.85 (d, *J* = 6.3 Hz, 2H), 8.14 (d, *J* = 7.8 Hz, 2H), 7.62 – 7.55 (m, 4H), 7.45 (t, *J* = 8.5 Hz, 2H), 7.35

(t, *J* = 7.5 Hz, 2H).**$^{13}C\{^{1}H\}$ NMR (126 MHz, $CDCl_3$)** δ 151.79, 145.63, 139.57, 126.50, 124.32, 121.23, 120.71, 120.68, 109.89.

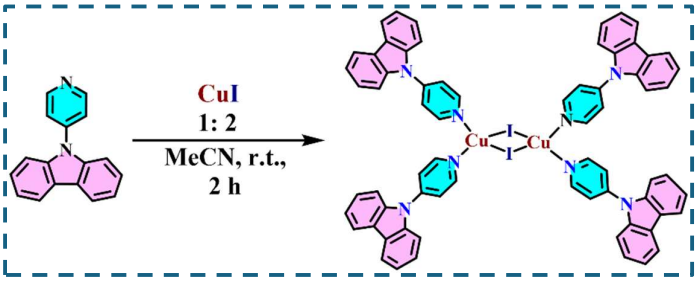


Scheme 1. Synthesis of **PyCbz**.

2.3 Synthesis of Complexes:

2.3.1 Synthesis of C1:

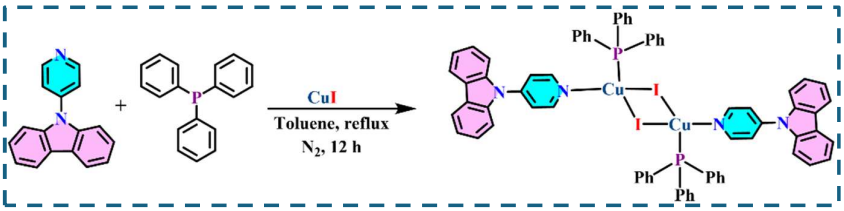
In a clean and oven-dried Schlenk tube, CuI (40 mg, 0.2049 mmol, 1 equiv) was dissolved in acetonitrile (5 mL) under an inert nitrogen atmosphere. After 5 minutes, **PyCbz** (150 mg, 0.6147 mmol, 3 equiv) was added to the reaction mixture, which was stirred for an additional 2 hours. Upon completion of the reaction, the mixture was allowed to reach room temperature and subsequently concentrated under reduced pressure to remove the solvent. The resulting crude product was collected as a light-green solid, affording the desired complex in more than 78% yield.



Scheme 2. Synthesis of **C1**.

2.3.2 Synthesis of C2:

In an oven-dried Schlenk tube, CuI (77.9 mg, 0.409 mmol, 1 equiv) and triphenylphosphine (PPh_3, 107.15 mg, 0.409 mmol, 1 equiv) were dissolved in toluene (5 mL) under an inert atmosphere. The reaction mixture was refluxed with continuous stirring for 50 minutes. Subsequently, **PyCbz** (100 mg, 0.409 mmol, 1 equiv) was introduced into the reaction medium and further stirred for an additional 12 hours under an inert atmosphere. After completion of the reaction, the solvent was removed under reduced pressure using a rotary evaporator. The crude residue was dissolved in 1 mL of DCM, and the pure product was recrystallized by slow diffusion of n-hexane into the solution. An off-white-coloured solid was obtained with over 75% yield. **^{1}H NMR (500 MHz, $CDCl_3$)** δ 8.90 (d, *J* = 6.4 Hz, 4H), 8.13 (d, *J* = 7.6 Hz, 4H), 7.56 (s, 4H), 7.54 (d, *J* = 3.5 Hz, 6H), 7.51 (d, *J* = 8.4 Hz, 10H), 7.44 (t, *J* = 7.7 Hz, 4H), 7.34 (t, *J* = 7.4 Hz, 10H), 7.26 (t, *J* = 6.8 Hz, 13H). **^{13}C{^{1}H} NMR (126 MHz, $CDCl_3$)** δ 151.97, 145.95, 139.43, 134.30, 133.09, 132.85, 129.82, 128.61, 126.58, 124.45, 121.43, 120.73, 109.93. **^{31}P{^{1}H} NMR (202 MHz, $CDCl_3$)** δ 5.43. **Melting point:** 201 °C.

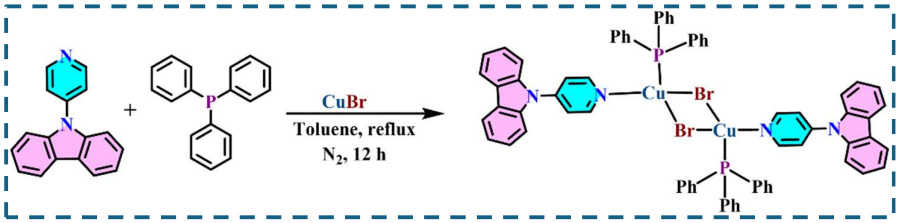


Scheme 3. Synthesis of **C2**.

2.3.3 Synthesis of C3:

Similar to **C2**, **C3** was also synthesized following the same procedure. In a clean and oven-dried Schlenk tube, CuBr (58.69 mg, 0.409 mmol, 1 equiv) and PPh_3 (107.15 mg, 0.409 mmol, 1 equiv) were dissolved in toluene (5 mL) under an inert nitrogen atmosphere. The reaction mixture was refluxed with continuous stirring for 50 minutes. Subsequently,

PyCbz (100 mg, 0.409 mmol, 1 equiv) was introduced into the reaction medium and further stirred for an additional 12 hours under an inert atmosphere. After completion of the reaction, the solvent was removed under reduced pressure using a rotary evaporator. The crude residue was dissolved in 1 mL of DCM, and the pure product was recrystallized by slow diffusion of n-hexane into the solution. A light green solid was obtained in over 82% yield. **^{1}H NMR (500 MHz, $CDCl_3$)** δ 8.89 (s, 4H), 8.10 (d, *J* = 8.1 Hz, 4H), 7.51 (q, *J* = 9.2 Hz, 18H), 7.42 (d, *J* = 7.8 Hz, 4H), 7.32 (d, *J* = 7.5 Hz, 12H), 7.27 (d, *J* = 7.8 Hz, 12H). **^{13}C{^{1}H} NMR (126 MHz, $CDCl_3$)** δ 152.35, 139.61, 134.43, 133.28, 133.01,132.52, 130.24, 129.03, 126.87, 124.75, 121.77, 120.99, 110.20. **^{31}P{^{1}H} NMR (202 MHz, $CDCl_3$)** δ -3.85. **Melting point:** 204 °C.

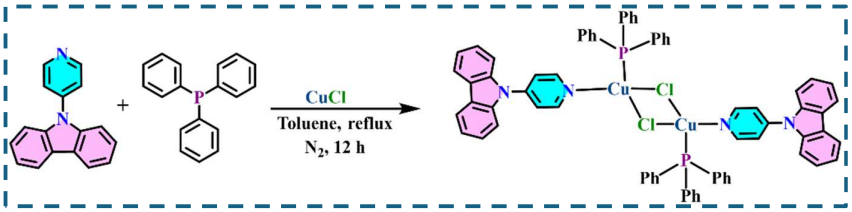


Scheme 4. Synthesis of **C3**.

2.3.4 Synthesis of C4:

Similar to **C2** and **C3**, **C4** was also synthesized using the same procedure. In a clean and oven-dried Schlenk tube, CuCl (40.49 mg, 0.409 mmol, 1 equiv) and PPh_3 (107.15 mg, 0.409 mmol, 1 equiv) were dissolved in toluene (5 mL) under an inert nitrogen atmosphere. The reaction mixture was refluxed with continuous stirring for 50 minutes. Subsequently, **PyCbz** (100 mg, 0.409 mmol, 1 equiv) was introduced into the reaction medium and further stirred for an additional 12 hours under an inert atmosphere. After completion of the reaction, the solvent was removed under reduced pressure using a rotary evaporator. The crude residue was dissolved in 1 mL of

DCM, and the pure product was recrystallized by slow diffusion of n-hexane into the solution. A green solid was obtained in over 86% yield. **^{1}H NMR (500 MHz, $CDCl_3$)** δ 8.89 (s, 4H), 8.10 (d, *J* = 8.1 Hz, 4H), 7.51 (q, *J* = 9.2 Hz, 18H), 7.42 (d, *J* = 7.8 Hz, 4H), 7.32 (d, *J* = 7.5 Hz, 12H), 7.27 (d, *J* = 7.8 Hz, 12H). **^{13}C{^{1}H} NMR (126 MHz, $CDCl_3$)** δ 152.35, 139.61, 134.43, 133.28, 133.01, 132.52, 130.24, 129.03, 126.87, 124.75, 121.77, 120.99, 110.20. **^{31}P{^{1}H} NMR (202 MHz, $CDCl_3$)** δ -2.00. **Malting point-** 202 °C.



Scheme 5. Synthesis of **C4**.

Chapter 3: RESULTS AND DISCUSSION

3.1 Characterization:

3.1.1 Characterization of Ligand:

3.1.1.1 Characterization of PyCbz:

PyCbz was synthesized by following a reported procedure (Scheme 1).(Morofuji et al., 2019) The product is characterized by ^{1}H and $^{13}C\{^{1}H\}$ NMR spectroscopy. The experimentally obtained NMR spectra matched the reported pattern, confirming the formation of **PyCbz** (Figures 6 & 7).

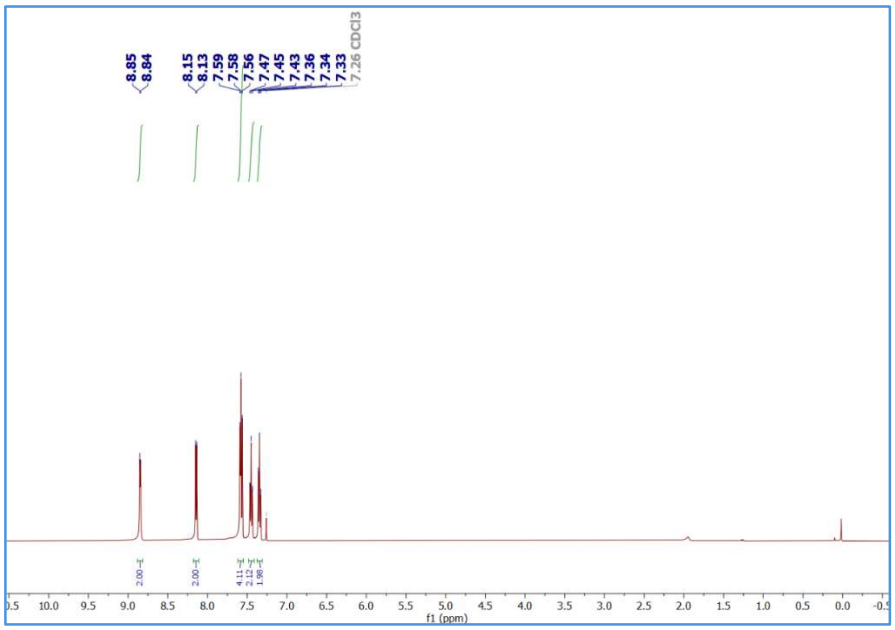


Figure 6. ^{1}H NMR of **PyCbz**.

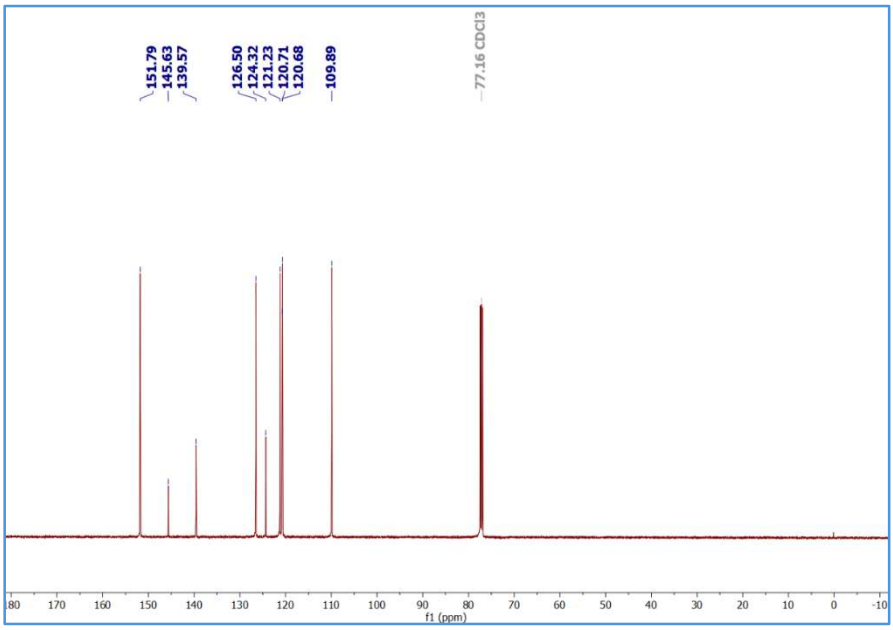


Figure 7. $^{13}C\{^{1}H\}$ NMR of **PyCbz**.

3.1.2 Characterization of the complexes:

3.1.2.1 Characterization of C1:

C1 was synthesized according to Scheme 2. The product was collected as a yellow solid with 78% yield. Due to poor solubility, NMR studies of the product were not possible. Single crystals of the complex were obtained by the slow evaporation of DMSO with in the 15-20 days. SCXRD analysis illustrates that the crystallization of **C1** occurs as a dimeric Cu_2I_2**PyCbz**$_4$ complex with a monoclinic *I2/a* space group (Figure 8). A DMSO molecule is co-crystalized in the single crystal of the complex. The dimeric unit consists of a diamond-shaped Cu_2I_2 core with **PyCbz** symmetrically coordinated to it. Each copper center is bonded to two nitrogen atoms of the pyridyl group of the ligand and two μ_2-bridged iodide atoms, satisfying the tetra valency of Cu(I). SCXRD analysis confirms the product formation and structure of **C1**. The separation between the two copper centers in the complex is 2.625Å (Figure 9). This distance is smaller than the van der Waals radius of copper (2.8 Å), indicating the presence of intramolecular cuprophilic

interaction in the complex. Further, PXRD results exhibits sharp peaks, corroborating the crystallinity of **C1** (Figure 10). The peaks are in good agreement with the simulated pattern, depicting the bulk phase purity of the powder compound.

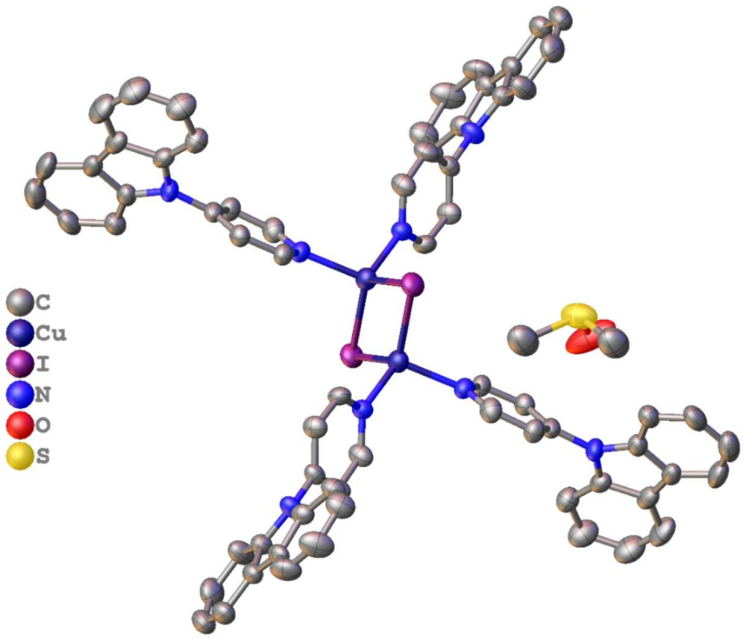


Figure 8. Single crystal structure of **C1** (H-atoms are omitted for clarity).

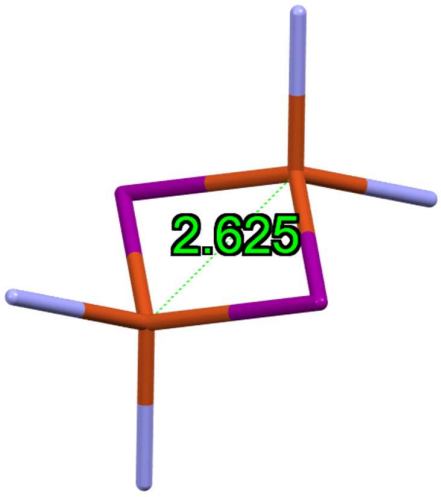


Figure 9. Structural representation of **C1** crystal highlighting the Cu···Cu separation (Å).

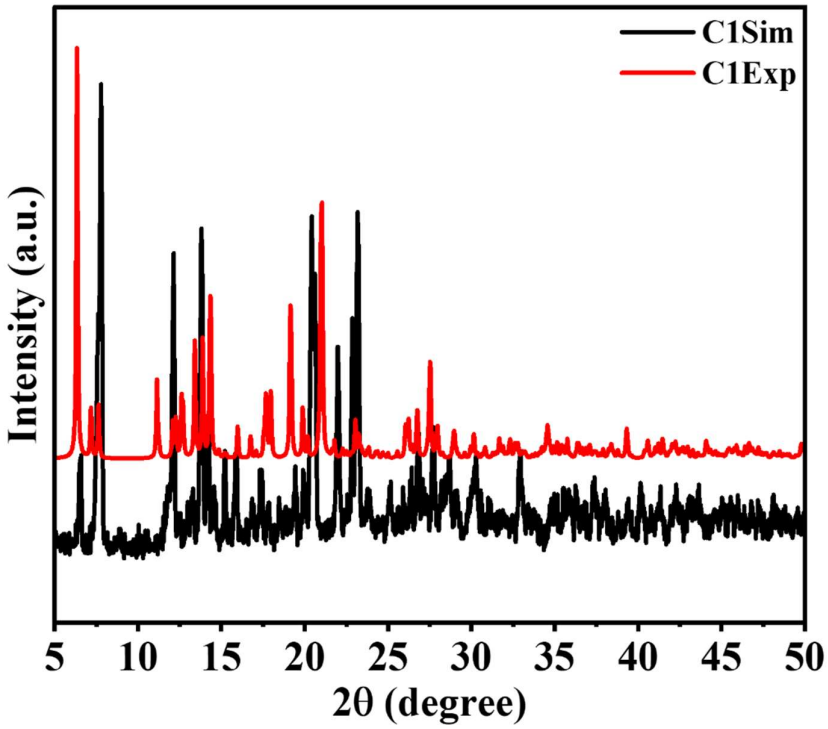


Figure 10. Comparison of the experimental and simulated PXRD patterns of **C1.**

3.1.2.2 Characterization of C2:

C2 was synthesized as per Scheme 3. The product was collected as an off-white solid with 75% yield. The product formation was confirmed by multinuclear NMR. The ^{1}H NMR spectrum of **C2** exhibits two distinct doublets at δ 8.90 and δ 8.13 ppm, which are attributed to the pyridyl protons of the **PyCbz** moiety (Figure 11). A multiplet centered around δ 7.52 ppm corresponds to the ortho protons of the phenyl ring and the meta protons (with respect to nitrogen) of the carbazole unit. Additionally, the para protons of the carbazole group appear as a multiplet at δ 7.44 ppm.

The signals observed in the range δ 7.34-7.26 ppm are assigned to the meta and para protons of the phenyl rings of PPh_3, along with the ortho protons of the carbazole moiety. The $^{13}C\{^{1}H\}$ NMR spectrum of **C2** displays peaks in the range of δ 109-152 ppm, consistent with the expected carbon environments (Figure 12). Furthermore, the $^{31}P\{^{1}H\}$ NMR spectrum shows a single peak at δ 5.43 ppm, indicating the

symmetric coordination of the two PPh_3 ligands around the metal center (Figure 13). **C2** was crystallized by slow diffusion of a DCM/n-hexane mixture, yielding SCXRD-quality transparent crystals. On analyzing the SCXRD structure, **C2** features a dimeric Cu_2I_2 core, similar to **C1**, with a slight modification in the coordination environment around each copper center (Figure 14). In **C2**, two **PyCbz** are replaced by two PPh_3. Consequently, each Cu(I) center is coordinated by the nitrogen atom from one **PyCbz**, phosphorus atom from one PPh_3, and two μ_2-bridging iodides, thereby retaining a tetrahedral coordination geometry. The crystallinity and bulk-phase purity of the product is confirmed by the PXRD analysis (Figure 15).

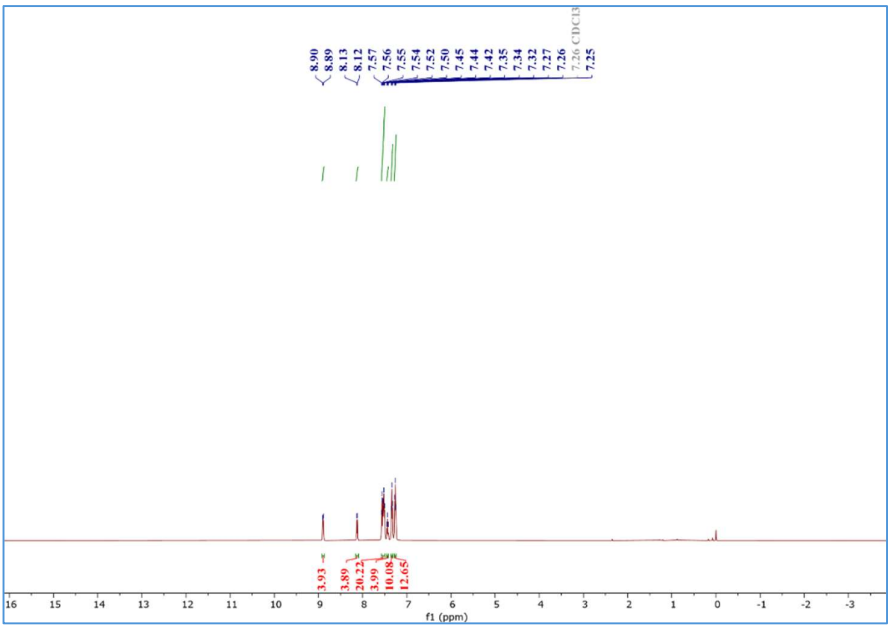


Figure 11. ^{1}H NMR of **C2**.

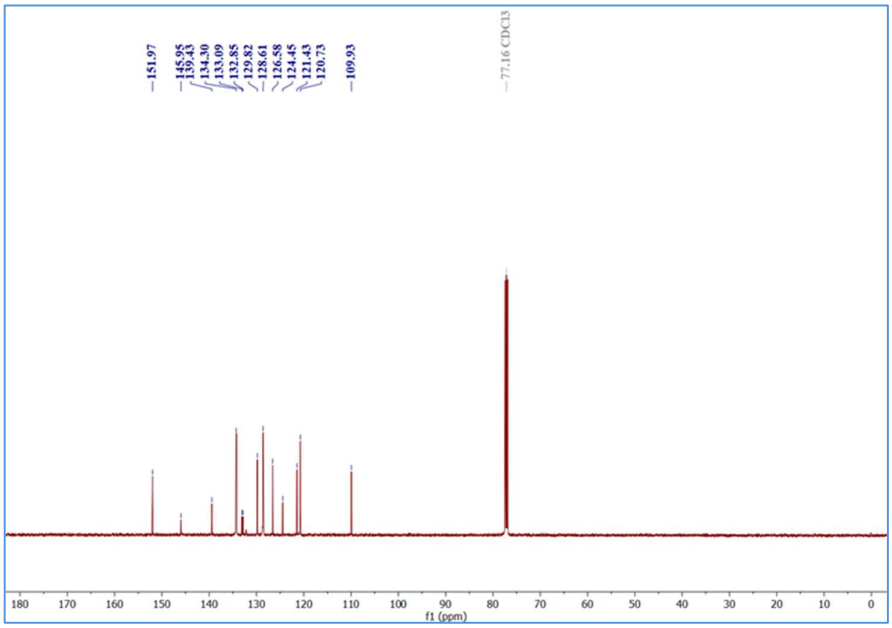


Figure 12. $^{13}C\{^{1}H\}$ NMR of **C2**.

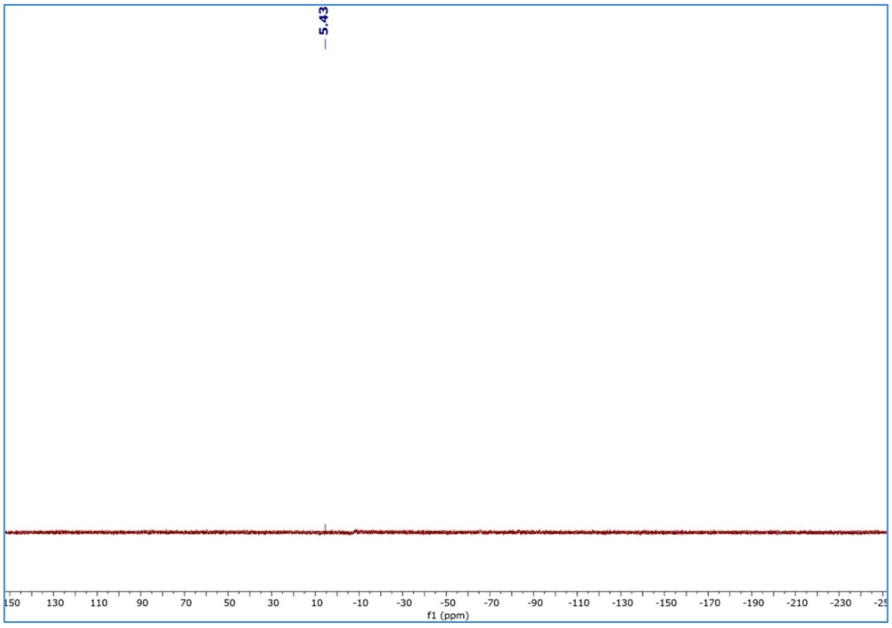


Figure 13. $^{31}P\{^{1}H\}$ NMR of **C2**.

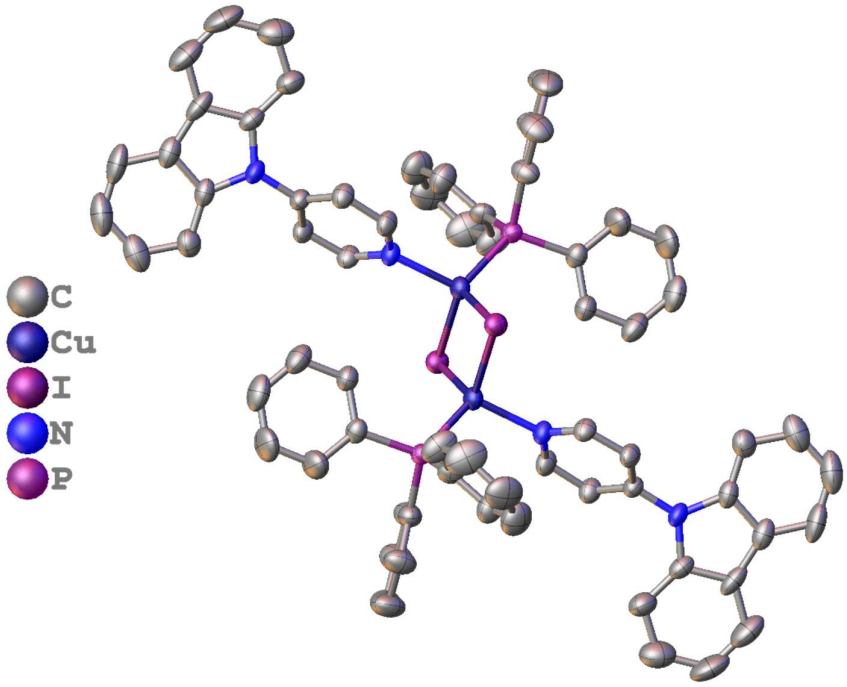


Figure 14. Single crystal structure of **C2** (H-atoms are omitted for clarity).

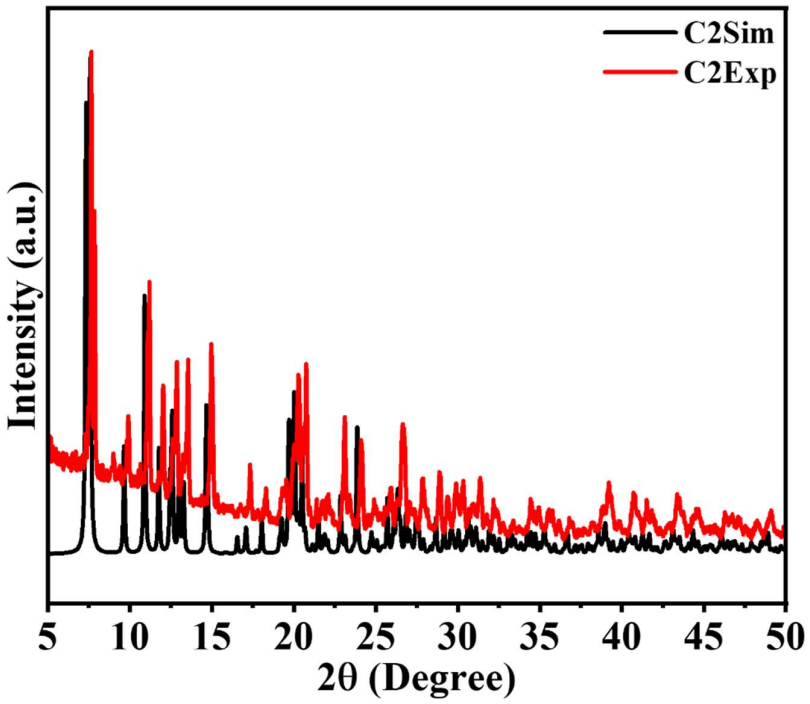


Figure 15. Comparison of the experimental and simulated PXRD patterns of **C2.**

3.1.2.3 Characterization of C3:

C3 was synthesized as per Scheme 4. The product was collected as an off-white solid with 82% yield. The product formation was confirmed by multinuclear NMR. A downfield shift in the δ value was observed compared to **PyCbz**, suggesting the coordination of **PyCbz** with copper (Figure 16). Further, $^{13}C\{^{1}H\}$ and $^{31}P\{^{1}H\}$ NMR show a similar pattern to that observed for **C2**, hinting at the presence of similar structural features (Figures 17 & 18). **C3** was crystallized by slow diffusion of a DCM/n-hexane mixture, yielding SCXRD-quality light-yellow crystals. SCXRD analysis shows **C3** crystallizes as a dimer, with a Cu_2Br_2 rhombic unit and $Cu_2Br_2(PPh_3)_2$**PyCbz**$_2$ as the formula unit (Figure 19). The crystallinity and bulk-phase purity of the product are confirmed by the PXRD analysis (Figure 20).

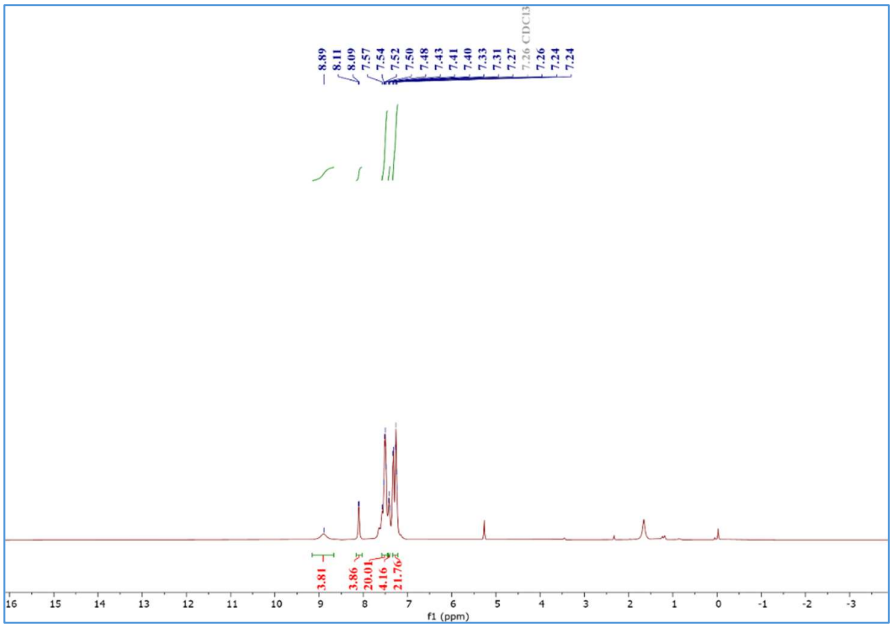


Figure 16. ^{1}H NMR of **C3**.

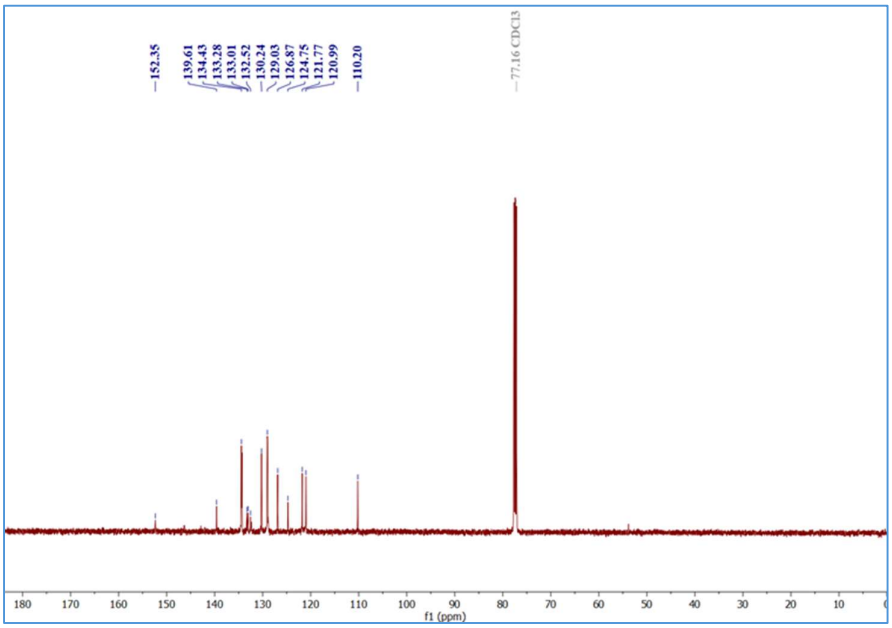


Figure 17. $^{13}C\{^{1}H\}$ NMR of **C3**.

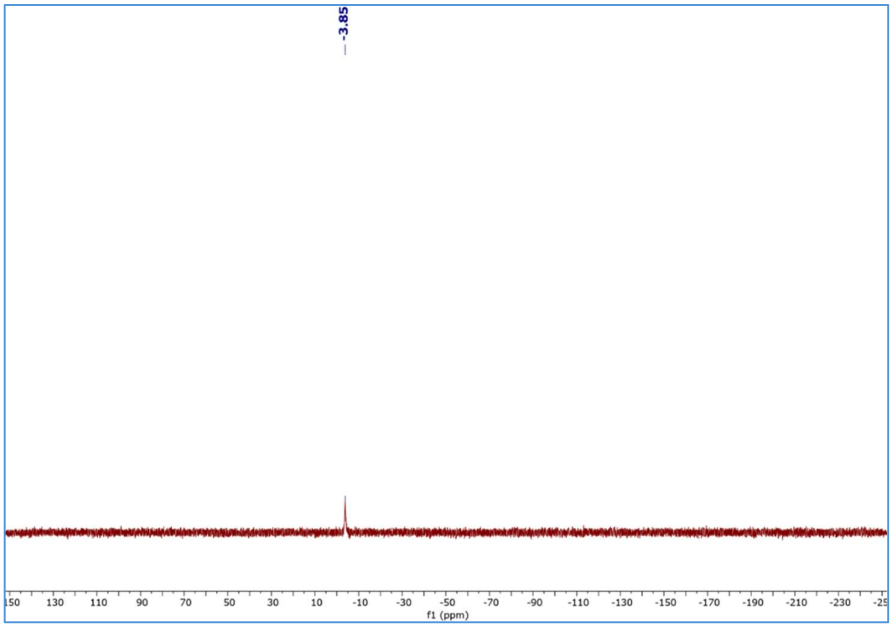


Figure 18. $^{31}P\{^{1}H\}$ NMR of **C3**.

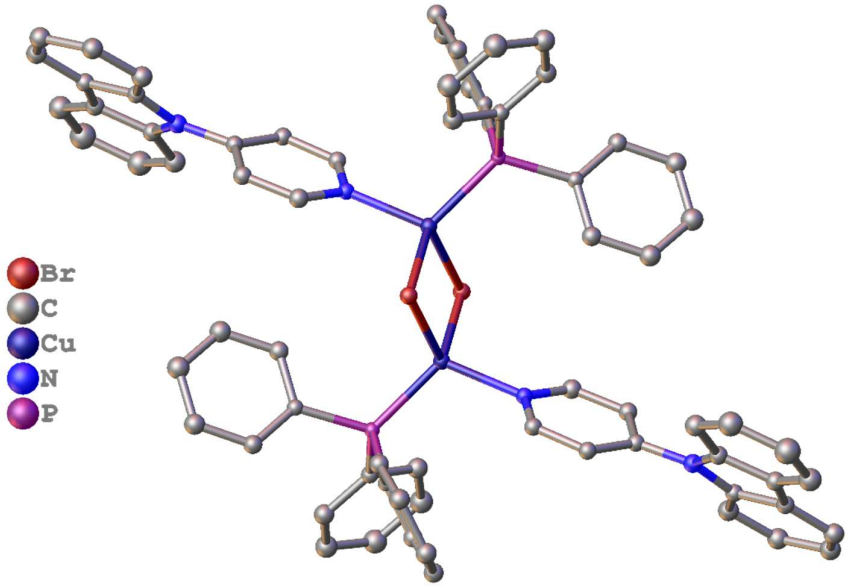


Figure 19. Single crystal structure of **C3** (H-atoms are omitted for clarity).

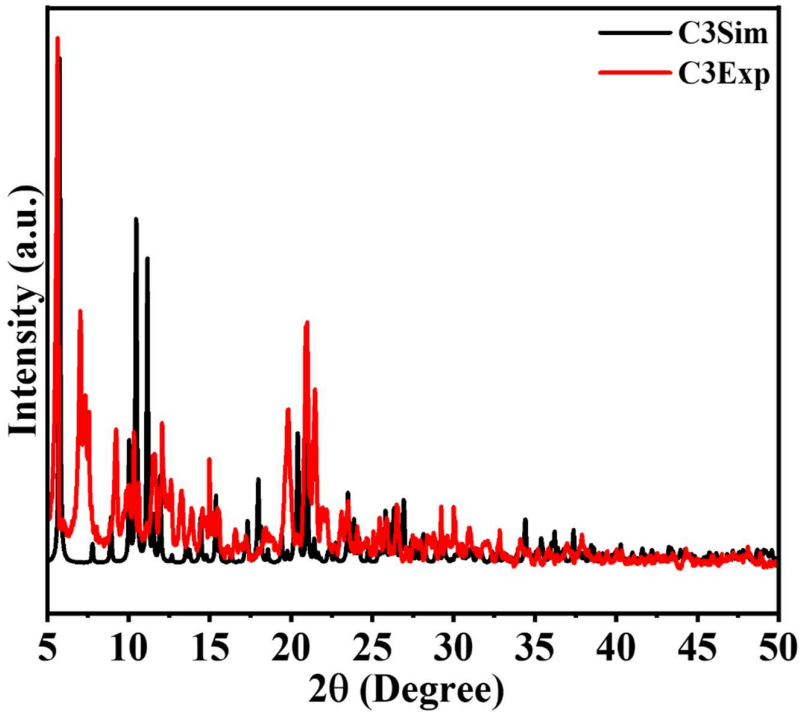


Figure 20. Comparison of the experimental and simulated PXRD patterns of **C3.**

3.1.2.4 Characterization of C4:

C4 was synthesized as per Scheme 5. The product was collected as an off-white solid with 86% yield. The product formation was confirmed by multinuclear NMR analysis. A downfield shift in the δ value was observed compared to **PyCbz**, suggesting the coordination of **PyCbz** with copper (Figure 21). Further, $^{13}C\{^{1}H\}$ and $^{31}P\{^{1}H\}$ NMR spectra show a pattern similar to that observed for **C2**, hinting at the presence of similar structural features (Figures 22 & 23). **C4** was crystallized by slow diffusion of a DCM/n-hexane mixture, yielding SCXRD-quality light-yellow crystals. SCXRD analysis shows **C4** crystallizes as a dimer, with a Cu_2Cl_2 rhombic unit and $Cu_2Cl_2(PPh_3)_2$**PyCbz**$_2$ as the formula unit (Figure 24). The crystallinity and bulk-phase purity of the product are confirmed by the PXRD analysis (Figure 25).

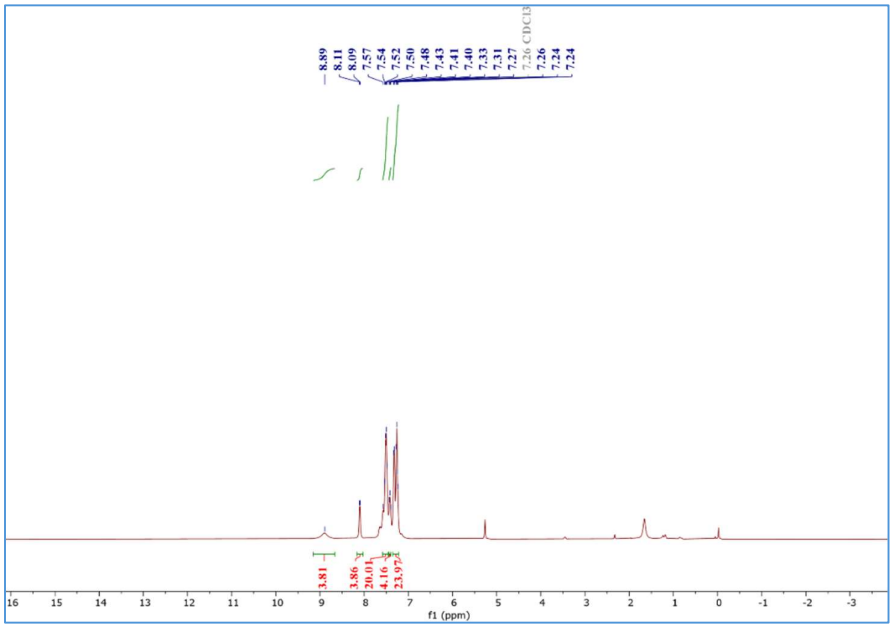


Figure 21. ^{1}H NMR of **C4**.

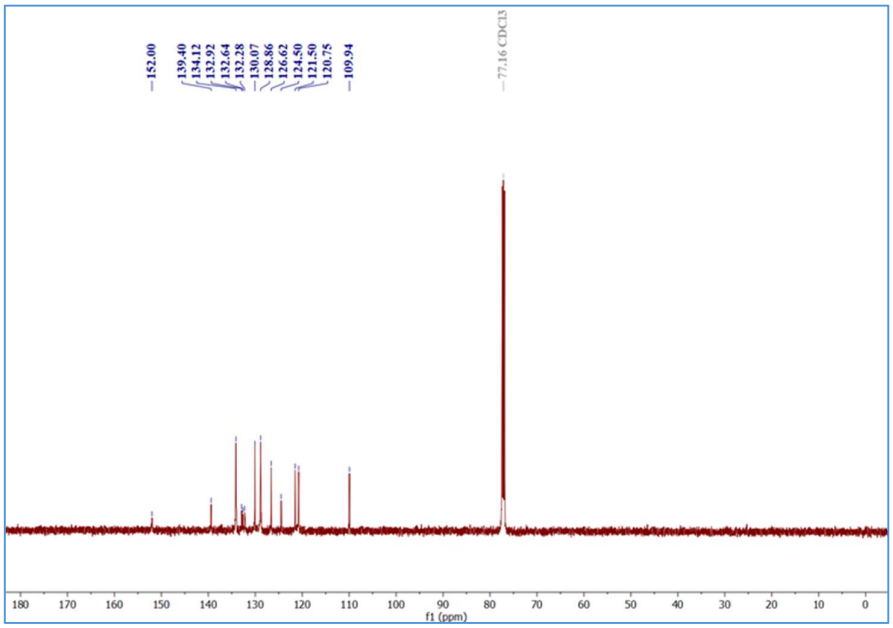


Figure 22. $^{13}C\{^{1}H\}$ NMR of **C4**.

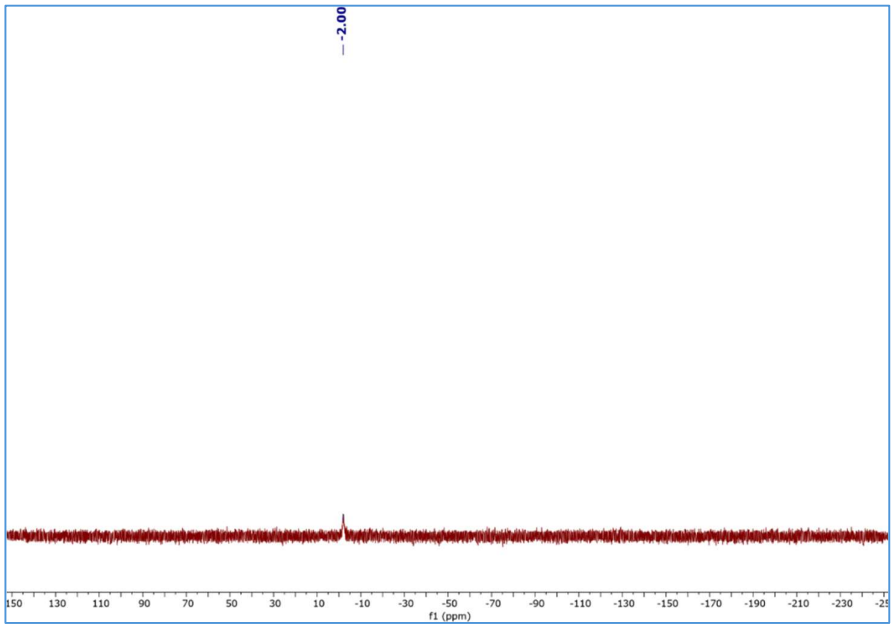


Figure 23. $^{31}P\{^{1}H\}$ NMR of **C4**.

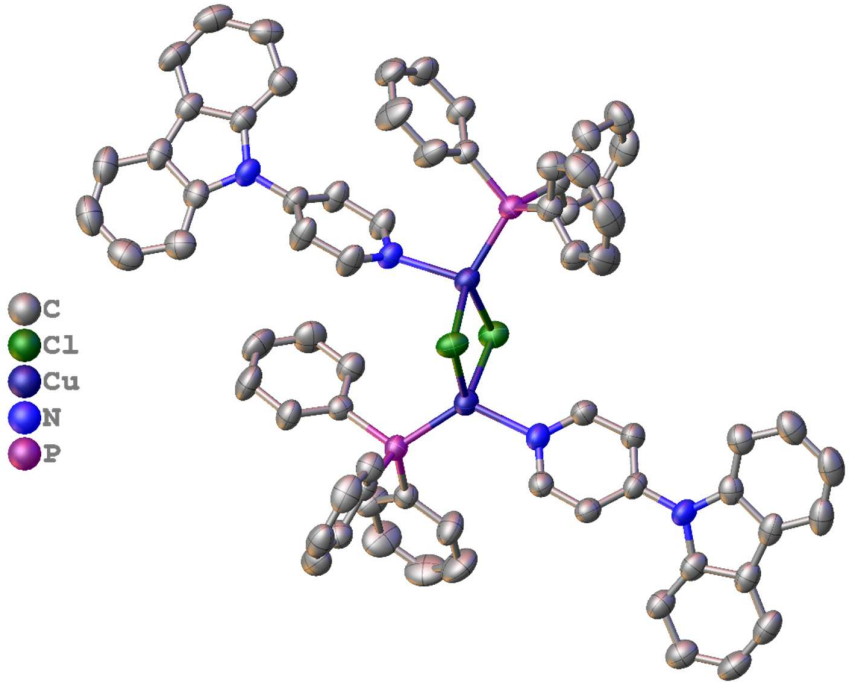


Figure 24. Single crystal structure of **C4** (H-atoms are omitted for clarity).

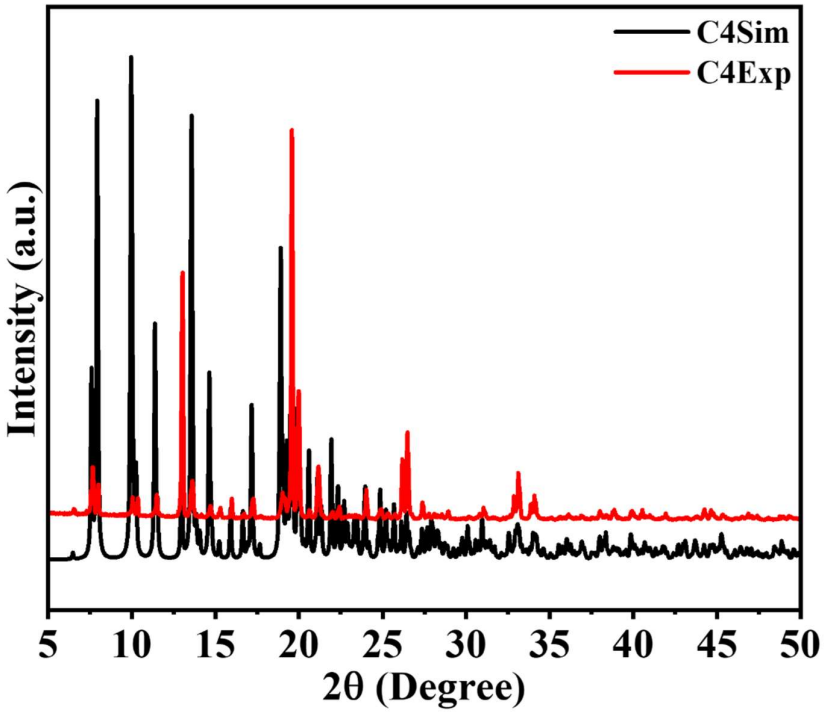


Figure 25. Comparison of the experimental and simulated PXRD patterns of **C4.**

3.2 Photophysical Study:

3.2.1 Solid State absorption studies:

The Solid-state UV-Vis DRS of the synthesized **PyCbz** and **C1-C4** was performed on powder samples over the range of 200-800 nm (Figure 26). The spectra show a broad band between 275 and 460 nm. The absorption spectrum of **PyCbz** consists of two bands centered at approximately 307 and 340 nm, which can be assigned to π→π* and n→π* transitions, respectively. The absorption spectrum of **C1** exhibits two main peaks at 337 nm and 397 nm. Complexes **C2-C4** showed an absorption pattern similar to that of **C1**, with the absorption band maxima in a similar range. The comparison of the absorption spectra of the ligand with those of the synthesized complexes reveals similar spectral features, suggesting that the observed absorption bands of the complexes likely originate from ligand-centered transitions. *[34-36]* The absorption maxima of the complexes exhibit a bathochromic shift relative to **PyCbz**, which may be attributed to the perturbations in molecular orbitals upon complexation. *[37]*

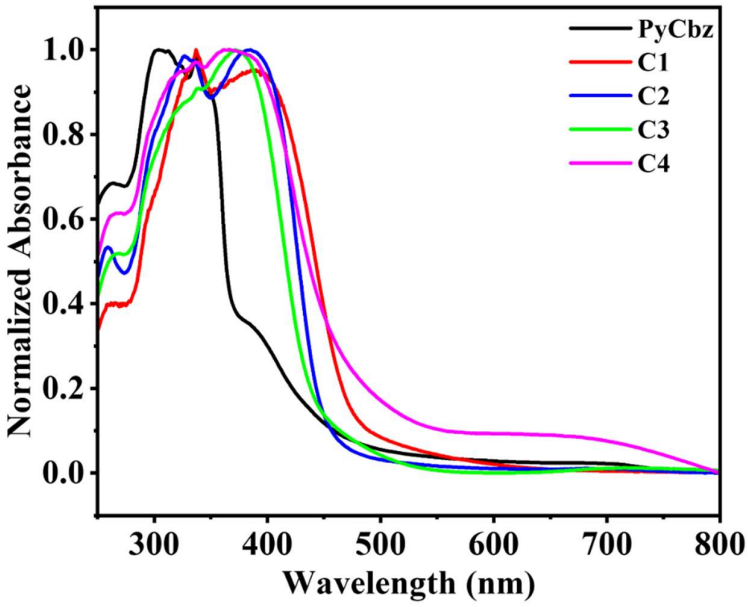


Figure 26. UV-Vis DRS of **PyCbz** and **C1-C4**.

3.2.2 Photophysical study of C1-C4:

Following the electronic characterization of **PyCbz** and its corresponding synthesized complexes, the solid-state PL of the complexes **C1**-**C4** was recorded at room temperature. The corresponding excitation-emission maxima, PLQY, decay times, and other photophysical properties are listed in Table 1.

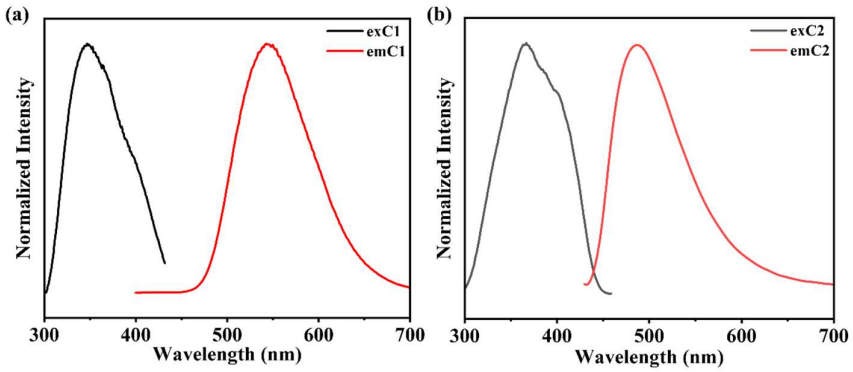


Figure 27 Solid-state PL spectrum of **C1**-**C2** recorded at room temperature.

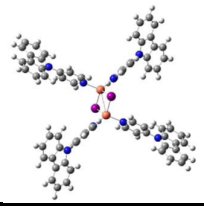
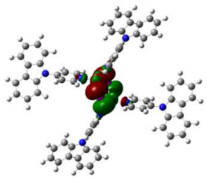
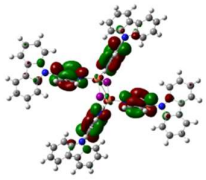
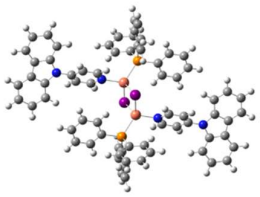
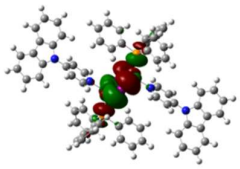
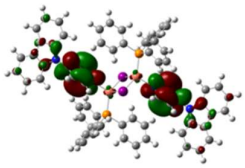
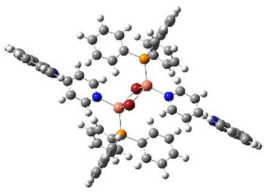
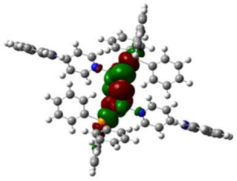
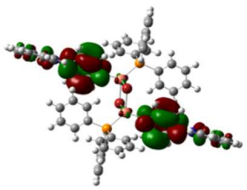
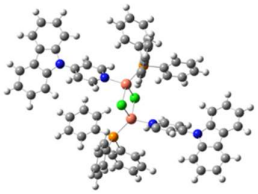
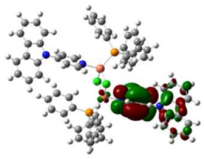
C1 exhibits a bright green emission under UV irradiation (λ = 365 nm) (Figure 28 on-set image). PL study showed an intense emission band spanning 470-580 nm (fwhm = 96 nm), centered at 545 nm (Figure 27a & Table 1). The complex exhibited excellent luminescence properties, with a PLQY of 61%. Further, the time-resolved decay measurements showed a lifetime of 12.12 µs. This prolonged microsecond lifetime rules out fluorescence involvement in the emission mechanism, and the excited-state relaxation may occur via phosphorescence or TADF. *[38]*

Table 1. Summary of the photophysical properties of **C1**-**C4**.

Complex	300 K						77 K			ΔEst (eV)
	λex (nm)	λem (nm)	τ (μs)	Θ	Kr (10^6) (s^{-1})	Knr (10^6) (s^{-1})	λex (nm)	λem (nm)	τ (μs)	
C1	345	545	12.12	61	0.0501	0.0323	365	541	15.98	0.013
C2	365	486	10.29	90	0.0870	0.0098	367	496	18.19	0.052
C3	365	542	13.32	66	0.0499	0.02520	365	553	53	0.170
C4	365	561	12.57	51	0.0405	0.03900	367	582	27.32	0.239

To support the observed phenomenon theoretically, the DFT calculations were performed. For the study, the SCXRD structures were used as initial geometries for the subsequent structural optimization. The analysis exhibits that the HOMO is localized on the Cu_2I_2 core, while the LUMO is distributed over the **PyCbz** ligands (Table 2). This spatial orbital distribution suggests (M+X)LCT characteristics of the excited state. This distant positioning of the FMOs favors high charge-transfer properties and supports the high PLQY observed. *[38,39]* Furthermore, the presence of cuprophilic interactions is expected to introduce significant Cu···Cu bonding character in the excited state, leading to the existence of low-lying ^{3}CC excited states. *[39,40]* Although the ^{3}CC state is initially higher in energy, it undergoes substantial structural relaxation in the excited state, leading to emission at longer wavelengths than the ^{3}(M+X)LCT state. Both the ^{3}CC and ^{3}(M+X)LCT states are often closely spaced, and there is a possible involvement of both states in the relaxation. *[41,42]*

Table 2. DFT optimized structure and FMOs for **C1**-**C4**.

DFT optimized figures	HOMO	LUMO
C1		
		
C2		
		
C3		
		
C4		
		

At room temperature, the available thermal energy can promote non-radiative decay transitions, complicating the determination of the dominant emissive states. In contrast, at low temperatures, the suppression of molecular motions minimizes the non-radiative losses and enables a clearer understanding of the emission mechanism. *[43]* This inspires a TDPL

study of **C1**. Accordingly, the solid-state emission and time-resolved decay measurements were recorded from 10 K to 300 K at regular intervals (Figure 28a and b). As the temperature is decreased, the emission maxima shift to shorter wavelengths relative to room temperature. This shift remains negligible up to 150 K but becomes more pronounced at lower temperatures, with the emission maxima reaching 533 nm at 10 K. This shift is accompanied by an increase in the emission intensity. The sequential blue shift of the emission maxima and the rise in intensity can be related to thermal equilibrium between ^{3}(M+X)LCT and ^{3}CC states. At room temperature, the ^{3}CC states are preferentially populated, leading to emission from low-energy ^{3}CC states. However, with the lowering of temperature, the insufficient thermal energy limits the ^{3}CC states and induces emission from ^{3}(M+X)LCT states.

Table 3. TDPL and temperature-dependent decay times of **C1**.

Temperature (K)	**λem (nm)**	**τ_{avg} (μs)**
10	533	16.51
30	536	16.47
50	539	16.42
70	541	15.98
90	542	15.70
110	543	15.67
130	545	15.47
150	548	15.26
170	548	15.11
200	548	14.82
230	548	13.33
260	548	13.26
300	548	12.12

The time-resolved decay measurements across the temperature range show a minimal increase in lifetime from 12.12 μs at 300 K to 16.51 μs at 10 K (Table 2 & Figure 28b). The microsecond emission lifetime is inconsistent with fluorescence. This monotonic increase in lifetime with decreasing temperature indicates suppression of non-radiative decay pathways. Notably, the decay time behavior does not follow a Boltzmann-type thermal distribution, thereby ruling out TADF and confirming that the emission is purely phosphorescent. Additionally, the relatively small variation in decay lifetimes across the temperature range supports the coexistence of both ^{3}(M+X)LCT and ^{3}CC states contributing to the overall emission process (Figure 28g). *[39]*

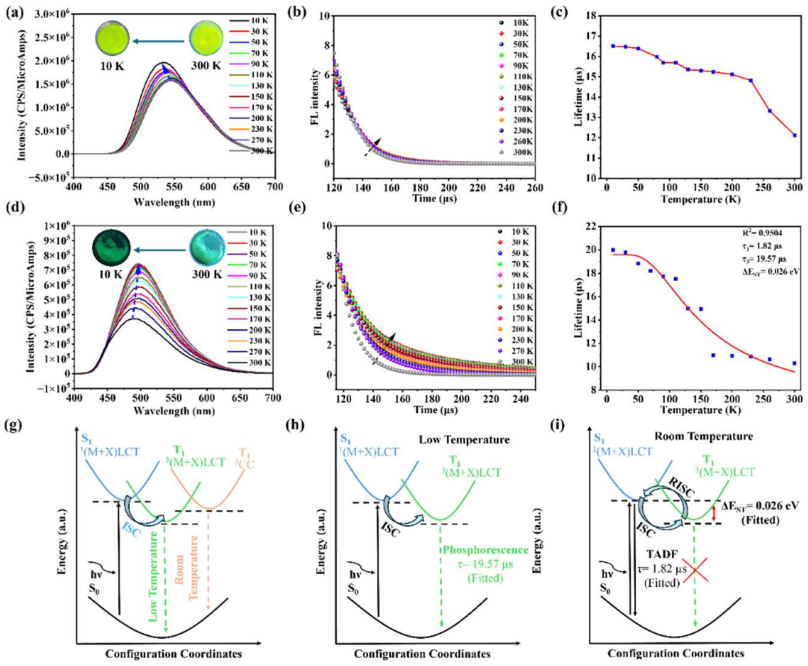


Figure 28. (a) TDPL spectrum of **C1** recorded between 10-300 K (On photoexcitation at 345 nm). **(b)** Temperature-dependent lifetime plots of **C1**. **(c)** Lifetime vs temperature plot for **C1**. **(d)** TDPL spectrum of **C2** recorded between 10-300 K (On photoexcitation at 365 nm). **(e)** Temperature-dependent lifetime plots of **C2**. **(f)** Lifetime vs temperature plot with Boltzmann-type fitting for **C2**. **(g)** Energy-level diagrams representing the excitation-emission mechanism of **C1** at both room temperature and low temperatures. **(h & i)** Energy-level diagrams

representing the excitation-emission mechanism of **C2** at room temperature and low temperature, respectively.

Afterward, the photoluminescent spectrum of **C2** was also studied. Upon photoexcitation at 365 nm, it exhibited a cyan-colored emission with a maximum at 489 nm. **C2** showed excellent emissive efficiency, with PLQY values reaching 90%, which is far higher than that recorded for **C1** (61%). This enhancement in PLQY upon introducing PPh_3 into the coordination system indicates the advantages of phosphine and supports the analogy considered during complex synthesis. The absence of cuprophilic interaction and the introduction of PPh_3 may alter the emission mechanism.

Table 3. TDPL and temperature-dependent decay times of **C2**.

Temperature (K)	**λem (nm)**	**τ_{avg} (μs)**
10	496	20.87
30	496	19.78
50	496	19.60
70	496	19.21
90	496	18.90
110	496	18.33
130	496	15.32
150	496	12.02
170	496	11.95
200	495	10.97
230	493	10.93
260	491	10.67
300	489	10.31

To evaluate the mechanism, TDPL studies were conducted. Upon cooling, **C2** exhibits a red shift in the emission maximum, in contrast to the blue shift observed for **C1** (Figure 28d & Table 3). At higher temperatures, a pronounced blue shift in emission is observed, which gradually diminishes

as temperature decreases. This trend is supported by a sharp increase in excited-state lifetime around 150 K (Figure 28e & Table 3), indicating that a higher-lying emissive state with a shorter lifetime is thermally populated at elevated temperatures. *[44]*

The temperature dependence of the emission lifetime was analyzed using a Boltzmann-type model:

$$r = \frac{3 + \exp(\frac{-\Delta E_{ST}}{k_B T})}{\frac{3}{\tau_3} + \frac{1}{\tau_1}\exp(\frac{-\Delta E_{ST}}{k_B T})} \qquad \textbf{eq. (I)}$$

where ΔE_{ST} represents the singlet-triplet energy gap between S_1 and T_1 states, kB is the Boltzmann constant, T is the absolute temperature, and τ_1 and τ_3 correspond to the lifetimes of low-lying singlet and triplet states, respectively (eq. (I)). *[45-47]* Fitting of the experimental data yields a ΔE_{ST} value of 0.029 eV, indicating a small singlet-triplet energy gap conducive to reverse intersystem crossing (RISC) (Figure 28f). The fitted triplet-state lifetime (τ_3 = 19.82 μs) closely matches the experimental value, supporting the validity of the model.

The small ΔE_{ST} facilitates efficient RISC, enabling repopulation of the singlet excited state at room temperature and promoting effective triplet harvesting. *[48-50]* These results indicate that the TADF dominates at room temperature, whereas phosphorescence becomes prominent at lower temperatures (Figure 28h and i). Consequently, the emission pathway shifts from triplet-state (T_1) emission at low temperatures to singlet-state (S_1) emission at higher temperatures, resulting in a blue-shifted emission maxima. The increase in emission intensity upon cooling is attributed to suppression of non-radiative decay pathways.

The emission mechanism was further supported by DFT calculations. It reveals that the HOMO is predominantly localized on the Cu_2I_2 core, along with contributions from the coordinated PPh_3 (Table 2). In contrast, the LUMO is primarily distributed over the pyridyl fragment of **PyCbz**, with minor contributions from the carbazole unit and the Cu(I) center. This

orbital distribution supports an (M+X) LCT character for the low-lying FMOs. *[35,51]*

To elucidate the effect of halide substitution on the emission characteristics, the photophysical properties of **C3** and **C4** were also investigated. Both the complexes exhibited bright visible emissions. **C3** shows green luminescence with a peak at 542 nm, whereas **C4** emits in the yellow region with a maximum at 562 nm (Figure 29). A systematic bathochromic shift is evident across the series from **C2** to **C4**, accompanied by a gradual color change from cyan to yellow. Structural parameters obtained from SCXRD and supported by DFT-optimized geometries reveal a progressive increase in Cu···Cu separation and distortion within the Cu_2X_2 core from **C2** to **C4**. Such structural variations are known to strongly influence the excited-state energy level in Cu(I) complexes. In particular, the lighter halides (Br^- and Cl^-) facilitate greater geometric relaxation upon excitation, leading to enhanced stabilization of the emissive triplet charge-transfer state. This interpretation is supported by the increasing Stokes shift observed across the series, reflecting a greater extent of excited-state reorganization. Consequently, despite the reduced polarizability of lighter halides, the increased structural relaxation dominates, leading to the observed red shift of the emission maxima.

Further, DFT calculations on **C3** and **C4** showed FMO distributions similar to those of **C2**, indicating a similar electronic arrangement across the complex (Table 2). The spatial separation between the HOMO (localized on the Cu_2X_2 core) and the LUMO (on **PyCbz**) supports the assignment of (M+X)LCT character. This is further corroborated by the relatively broad emission profiles (average FWHM ≈ 110 nm), typical of charge-transfer transitions. *[52]*

Among the series **C2**-**C4**, the PLQY follows a decreasing trend with **C2** (≈ 90%) > **C3** (≈ 66%) > **C4** (≈ 51%). This decrease may be correlated with the SOC of copper with halides. Iodide, being a heavier ion, exhibits a strong SOC. This leads to increased ISC and improved emissive

performance for **C2**. This interpretation aligns with the observed increase in Stokes shift (**C2** = 88 nm, **C3** = 116 nm, and **C4** = 130 nm), with **C3** showing the most pronounced shift. The combination of large fwhm values and significant Stokes shifts suggests substantial vibronic coupling in the excited state. This consequently leads to the red-shifting of emission maxima among the series from iodide to chloride (**C2-C4**)

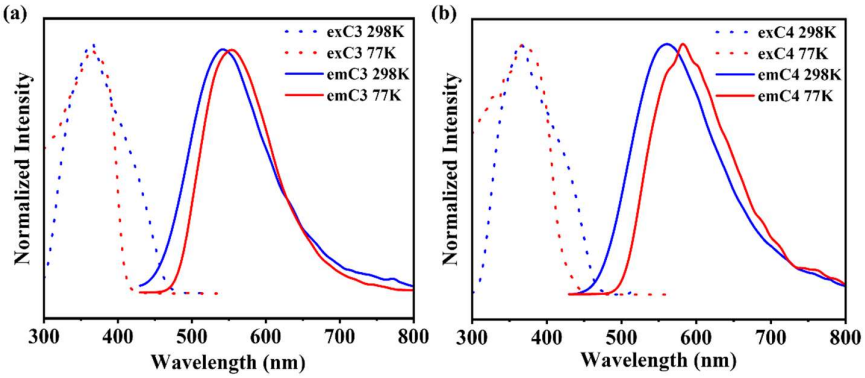


Figure 29. Solid-state photoluminescence spectrum of **(a) C3** and **(b) C4** at r.t. and 77K.

Further, to understand the emission mechanisms of **C3** and **C4**, the PL profile of both is also recorded at 77 K. Compared to room temperature, cooling results in a red shift in the emission maxima (Figure 29). This is accompanied by a notable increase in the decay time. For efficient TADF emitters, the ΔE_{ST} should be smaller than 0.3 eV. *[53,54]* The ΔE_{ST} values for **C2-C4** were estimated by subtracting the onsets of emission recorded at room temperature and at 77 K. Calculations yield the values in the range of 0.020 to 0.24 eV. Given the close resemblance of the structural and electronic features across **C2-C4**, a similar emission mechanism can be assumed. Accordingly, **C3** and **C4** are assigned to exhibit TADF at room temperature and phosphorescence at low temperatures. However, a discrepancy exists between the experimentally and theoretically calculated ΔE_{ST} values. The calculated values lie approximately between 0.50 and 0.65 eV, which is higher than the experimental values. This difference may arise from several factors, including dynamic experimental environments

thermal activation, structural relaxation, and the presence of solvents or other interfering agents in real conditions. *[35,55]*

3.3 Aggregation-Induced emission behavior of C2:

All the complexes are non-emissive in DMSO solution, but are highly emissive in the solid state. This suggests a potential AIE property in the complexes. Among the as-synthesized complexes, **C2** showed the highest PLQY (≈90 %), but in DMSO solution, its emission maximum decreased drastically. This pronounced contrasting behavior strongly motivated a detailed study of AIE. A series of DMSO-Water mixtures was prepared by varying the water fraction (f_w) from 5 to 95% (v/v%). Throughout this process, the concentration of the complexes in each mixture was maintained at 7.8 × 10^ (- 5) mol L^ (-1). The increase in the f_w is associated with the appearance of emission as seen in the photographic images (Figure 30a). To characterize this behavior, the photoluminescence spectrum of the mixture was recorded as a function of f_w with 365 nm photoexcitation (Figure 30b). Beyond 50%, a sharp rise in the emission intensity indicates the onset of aggregation.

To further study the size and surface charge of the aggregates, DLS and Zeta potential measurements are performed on the aggregated mixture (fw = 90%) (Figure 30c). DLS measurements showed a mean diameter of 134 nm, indicating the formation of nanoaggregates. Similarly, a low zeta potential of -14.3 mV indicates a strong tendency for aggregation of **C2**. In the solution form, the greater degree of motion facilitates the non-radiative decay, thereby quenching the emission. But in the aggregated state, an increasing water fraction leads to nanoaggregation, which restricts intermolecular motion and enhances emission. The presence of weak intermolecular interactions, such as π···π stacking, halogen···H, and π···H, also contributes to molecular rigidity.

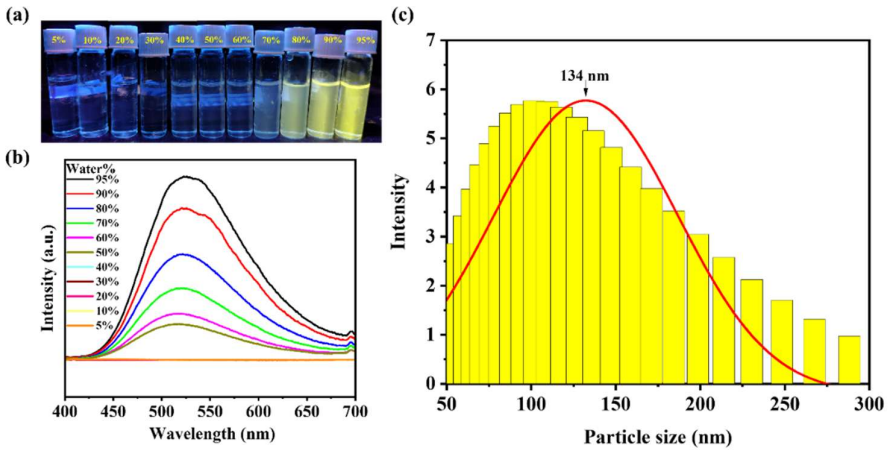


Figure 30. (a) The photographs of aggregated mixtures of **C2**, under UV light (λ= 365 nm), with the order of increasing f_w%. **(b)** The corresponding photoluminescence spectra with λ_{ex}= 365 nm. **(c)** DLS of an aggregated mixture of **C2** at f_w= 90%.

3.3 Film fabrication of C1 and the corresponding photophysical study:

The PL study of all the synthesized complexes showed excellent emissive properties, with high PLQYs. **C2** exhibited the highest PLQY (~90%), motivating further investigation of its film properties. A hybrid film was fabricated by using Polymethylmethacrylate (PMMA) and **C2** in a 95:5 wt.% ratio. The mixture is drop-casted onto the glass surface and left to dry for 10-12 h. The host alone is non-emissive, but the introduction of the dopant **C2** introduces emission. The photophysical properties of the film were analyzed by recording the PL spectrum upon photoexcitation at 330 nm. The film showed a broader spectrum and a slightly red-shifted emission maximum at 494 nm compared to the solid-state guest complex (Figure 31). In the film state, some very weak host-guest interactions, such as dipole-dipole or van der Waals forces, may induce moderate excited-state stabilization, leading to red-shifted emission. *[56]* The PLQY of the film was found to be 20%, which is lower than that in the powder state.

But even a small amount of material doping still exhibited good emissive efficiency.

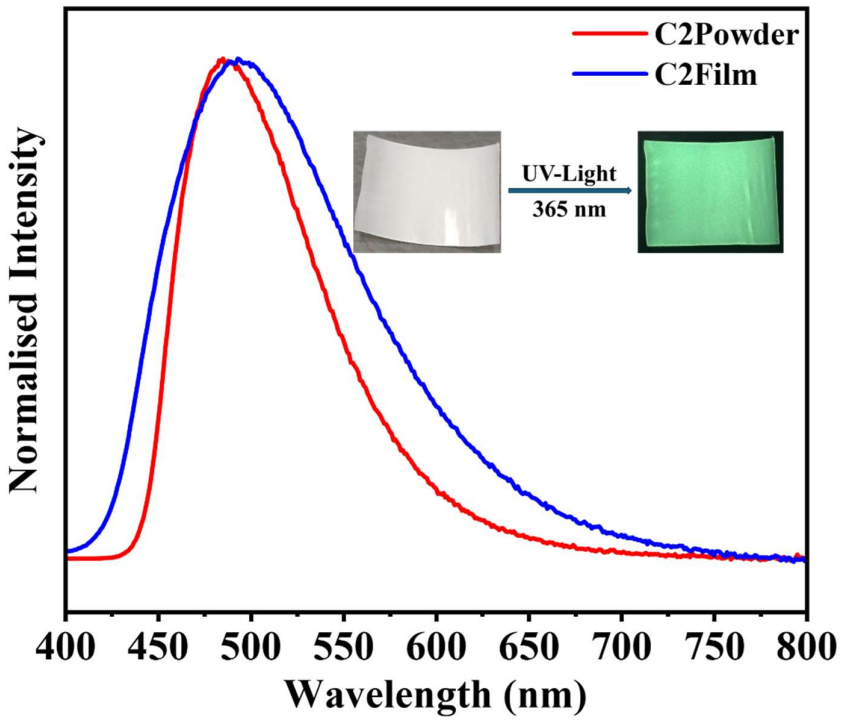


Figure 31. Comparison of the solid-state photoluminescent spectrum of the fabricated **C2** film and its solid powder.

Chapter 4: CONCLUSIONS AND FUTURE SCOPE:

4.1 Conclusions:

In this work, complex **C1** was synthesized using CuI and **PyCbz**. Further, a series of three heteroleptic complexes **C2**-**C4** incorporating **PyCbz** and PPh_3 ligands was successfully synthesized in good yields, and the structures are characterized by multinuclear NMR studies. SCXRD analysis of the complexes reveals a dimeric architecture with a rhombic Cu_2X_2 core. Also, the close proximity of the two copper units (2.625 Å) indicates the presence of cuprophilic interaction. **C1** exhibited bright green emission with a microseconds decay time (12.12 μs). Further, the DFT analysis indicates the position of HOMO and LUMO on the Cu_2I_2 core and **PyCbz**, respectively. This distinct FMO distribution indicates a mixed contribution from ^{3}CC and ^{3}(M+X)LCT to the charge-transfer mechanism. Furthermore, the TDPL of **C1** indicates phosphorescence as the emission mechanism. In contrast, the introduction of steric modulation in **C2** reduces the cuprophilic interaction. This reduction modifies charge transfer via ^{3}(M+X)LCT states. The TDPL study performed on **C2** indicates that the emission follows TADF at room temperature and phosphorescence at low temperatures. Further, in **C2**-**C4**, the systematic variation of halides from iodide to chloride induces a red shift in the emission maxima alongside a decrease in PLQY (90% → 51%). This reduction in emission efficiency may be attributed to enhanced non-radiative decay resulting from increased vibrational coupling in low-molecular-weight halides. Further, **C2** exhibited AIE property, with about 85% enhancement of emission intensity in a saturated aggregated solution (95%). The excellent emission efficiency of **C1** leads to its film fabrication using PMMA as a host material. Film provides structural stability and retains the material's intrinsic luminescence. This work sheds light on an efficient design of highly emissive Cu(I) complexes with effective triplet harvesting and opens a

way for the design and development of efficient materials for optoelectronic applications.

4.2 Future Scope:

Further, we will try to synthesize more coordination complexes by varying both the metal source and phosphine ligands. In this context, cuprous halides will be replaced by ionic cuprous systems like $[Cu(MeCN)_4]X$, X = (PF_6, ClO_4, BF_4, etc.). Similarly, bulkier monophosphines such as JohnPhos, SPhos, Xphos, tBuXphos, etc., and diphosphines such as POP and Xantphos will replace PPh_3. The thorough structural and photophysical study of the synthesized compounds will be performed. In addition, the detailed study of the structural changes occurring during **C2** aggregation and the mechanism of modification of the excited states that results in the shifting of emission will be investigated. Further, PMMA will be replaced by widely used host materials such as DMIC-TRZ and mCP. These host materials often enhance emission efficiency. Collectively, these investigations are expected to provide deeper insights into the structure-property relationships and facilitate the rational design of materials for optoelectronic applications.

5. REFERENCES:

[1] Amouri. H. (2023). Luminescent Complexes of Platinum, Iridium, and Coinage Metals Containing *N* -Heterocyclic Carbene Ligands: Design, Structural Diversity, and Photophysical Properties. Chem Rev, *123*(1), 230–270. (DOI:10.1021/acs.chemrev.2c00206)

[2] Baranov A. Yu., Rakhmanova M. I., Hei X., Samsonenko D. G., Stass D. V., Bagryanskaya, I. Yu., Ryzhikov, M. R., Fedin, V. P., Li, J., & Artem'ev, A. V. (2023). A new subclass of copper(I) hybrid emitters showing TADF with near-unity quantum yields and a strong solvatochromic effect. Chem Commun, *59*(20), 2923–2926. (DOI:10.1039/D3CC00119A)

[3] Barman D., Narang K., Gogoi R., Barman D., & Iyer P. K. (2022). Exceptional class of thermally activated delayed fluorescent emitters that display pure blue, near-IR, circularly polarized luminescence and multifunctional behaviour for highly efficient and stable OLEDs. J Mater Chem C, *10*(22), 8536–8583. (DOI:10.1039/D1TC05906H)

[4] Baruah K., Gogoi R., Iyer P. K., & Khatua S. (2026). Aggregation-Induced Emission and Thermally Activated Delayed Fluorescence in Sterically Encumbered Copper(I) Complexes of Diphosphine and Substituted Phenanthroline Ligands. Inorg Chem, *65*(1), 79–94. (DOI:10.1021/acs.inorgchem.5c03487)

[5] Beaudelot, J., Oger, S., Peruško, S., Phan, T.-A., Teunens, T., Moucheron, C., & Evano, G. (2022). Photoactive Copper Complexes: Properties and Applications. Chem Rev, *122*(22), 16365–16609(DOI:10.1021/acs.chemrev.2c00033)

[6] Chatterjee J., Chatterjee A., Tanwar R., Panwaria P., Saikia S., Ambhore M. D., Mandal P., & Hazra P. (2024). Activation of TADF in Photon Upconverting Crystals of Dinuclear Cu(I)-Iodide Complexes by Ligand Engineering. J Phys Chem Lett, *15*(23), 6069–6080. (DOI:10.1021/acs.jpclett.4c01122)

[7] Chen J., London H. C., Pattadar D., Worster C., Salpage S. R., Jakubikova E., Saavedra S. S., & Hanson K. (2025). Increasing excited state lifetimes of Cu(I) coordination complexes *via* strategic surface binding. Inorg Chem Front, *12*(3), 1295–1302.(DOI:10.1039/D4QI02410A)

[8] Dos Santos J. M., Hall D., Basumatary B., Bryden M., Chen D., Choudhary P., Comerford T., Crovini E., Danos A., De J., Diesing S., Fatahi M., Griffin M., Gupta A. K., Hafeez H., Hämmerling L., Hanover E., Haug J., Heil T., … Zysman-Colman E. (2024). The Golden Age of Thermally Activated Delayed Fluorescence Materials: Design and Exploitation. Chem Rev, *124*(24), 13736–14110. (DOI:10.1021/acs.chemrev.3c00755)

[9] El-Saady A. A., Farag A. a. M., Ibrahim M. A., Mansour A. M., El-Nahass M. M., Salah N., & Magar H. S. (2025). Exploring the Structural, Optical, and electrochemical behavior of semicarbazone pyranoquinoline ligand (PQMHC) and its Cu(II) complex for efficient hydrogen peroxide sensing. Sci Rep, *15*(1), 43587. (DOI:10.1038/s41598-025-29948-6)

[10] Feng G., & Liu B. (2018). Aggregation-Induced Emission (AIE) Dots: Emerging Theranostic Nanolights. Acc Chem Res, *51*(6), 1404–1414. (DOI:10.1021/acs.accounts.8b00060)

[11]Forni A., Malpicci D., Lucenti E., Zecchinello L., Colombo A., & Cariati E. (2025a). Recent advances in mono- and multi-nuclear photoluminescent Cu(I) complexes with nitrogen containing ligands and their stimuli responsiveness. Chem Sci, *16*(44), 20755–20805. (DOI:10.1039/D5SC04685H)

[12] Forni, A., Malpicci, D., Lucenti, E., Zecchinello, L., Colombo, A., & Cariati, E. (2025b). Recent advances in mono- and multi-nuclear photoluminescent Cu(I) complexes with nitrogen containing ligands and their stimuli responsiveness. Chem Sci, *16*(44), 20755–20805. (DOI:10.1039/D5SC04685H)

[13] Inai N., Yasuda T., Fujimoto K. J., & Yanai T. (2024). Extended theoretical modeling of reverse intersystem crossing for thermally activated delayed fluorescence materials. Sci Adv.

[14] Hagfeldt A., Boschloo G., Sun L., Kloo L., & Pettersson H. (2010). Dye-Sensitized Solar Cells. Chem Rev, *110*(11), 6595–6663. (DOI:10.1021/cr900356p)

[15] Idris M., Muthiah Ravinson D. S., Jung M. C., Haiges R., Djurovich P. I., & Thompson M. E. (2020). Highly Efficient Deep Blue Luminescence of 2-Coordinate Coinage Metal Complexes Bearing Bulky NHC Benzimidazolyl Carbene. *Front Chem*, *8*. (DOI:10.3389/fchem.2020.00401)

[16] Hofbeck T., Monkowius U., & Yersin H. (2015). Highly Efficient Luminescence of Cu(I) Compounds: Thermally Activated Delayed Fluorescence Combined with Short-Lived Phosphorescence. *J Am Chem Soc*, *137*(1), 399–404. (DOI:10.1021/ja5109672)

[17] Hong Y., Lam J. W. Y., & Tang B. Z. (2011). Aggregation-induced emission. Chem Soc Rev, *40*(11), 5361. (DOI:10.1039/c1cs15113d)

[18] Housecroft, C. E., & Constable, E. C. (2022). TADF: Enabling luminescent copper(I) coordination compounds for light-emitting electrochemical cells. J Mater Chem C, *10*(12), 4456–4482. (DOI:10.1039/D1TC04028F)

[19] Huang C.-H., Yang M., Chen X.-L., & Lu, C.-Z. (2021). Bright bluish-green emitting Cu(I) complexes exhibiting efficient thermally activated delayed fluorescence. *Dalton Trans*, *50*(15), 5171–5176. (DOI:10.1039/D0DT04424E)

[20] Jazzar R., Soleilhavoup M., & Bertrand G. (2020). Cyclic (Alkyl)- and (Aryl)-(amino)carbene Coinage Metal Complexes and Their Applications. *Chemical Reviews*, *120*(9), 4141–4168. (DOI:10.1021/acs.chemrev.0c00043)

[21] Kharabe L. S., Chaudhari K., Mishra A., & Raghuvanshi A. (2025). NHC stabilized two-coordinated mono- and bimetallic Cu(I) complexes: Ligand-directed emission and solvatochromism. J Organomet Chem, *1041*, 123841. (DOI:10.1016/j.jorganchem.2025.123841)

[22] Kitagawa H., Ozawa Y., & Toriumi K. (2010). Flexibility of cubane-like Cu4I4 framework: Temperature dependence of molecular structure and luminescence thermochromism of [Cu4I4(PPh3)4] in two

polymorphic crystalline states. Chem Commun, *46*(34), 6302. (DOI:10.1039/c0cc01434f)

[23] Lan L., & Zhang H. (2025). Red and Near-Infrared Emissive Organic Crystals: Molecular Design and Optoelectronic Applications. Angew Chem Int Ed, *64*(28), e202509140. (DOI:10.1002/anie.202509140)

[24] J., Küchle, F.-R., Mayer, H. A., Wesemann, L., & Yersin, H. (2013). Brightly Blue and Green Emitting Cu(I) Dimers for Singlet Harvesting in OLEDs. J Phys Chem A, *117*(46), 11823–11836. (DOI:10.1021/jp402975d)

[25] Li S., Zhou X., Xu L., Yu C., Liu J., Yan S., & Ren Z. (2026). Beyond 800 nm: Recent progress in high-performance near-infrared thermally activated delayed fluorescence based OLEDs. Chem Sci, *17*(10), 4863–4880. (DOI:10.1039/D5SC09087C)

[26] Li T.-Y., Zheng S.-J., Djurovich P. I., & Thompson M. E. (2024). Two-Coordinate Thermally Activated Delayed Fluorescence Coinage Metal Complexes: Molecular Design, Photophysical Characters, and Device Application. *Chem Rev*, *124*(7), 4332–4392.(DOI:10.1021/acs.chemrev.3c00761)

[27] Linfoot C. L., Leitl M. J., Richardson P., Rausch A. F., Chepelin O., White F. J., Yersin, H., & Robertson N. (2014). Thermally Activated Delayed Fluorescence (TADF) and Enhancing Photoluminescence Quantum Yields of $[Cu^{I}$ (diimine)(diphosphine)$]^{+}$ Complexes—Photophysical, Structural, and Computational Studies. Inorg Chem, *53*(20), 10854–10861. (DOI:10.1021/ic500889s)

[28] Liu J., Chen J., Dong Y., Yu Y., Zhang S., Wang J., Song Q., Li W., & Zhang C. (2020). The origin of the unusual red-shifted aggregation-state emission of triphenylamine-imidazole molecules: Excimers or a photochemical reaction? Mater Chem Front, *4*(5), 1411–1420. (DOI:10.1039/C9QM00737G)

[29] Liu Y., Li Y., Koo S., Sun Y., Liu Y., Liu X., Pan Y., Zhang Z., Du M., Lu S., Qiao X., Gao J., Wang X., Deng Z., Meng X., Xiao Y., Kim J. S., & Hong X. (2022). Versatile Types of Inorganic/Organic NIR-IIa/IIb Fluorophores: From Strategic Design toward Molecular Imaging and Theranostics. Chem Rev, *122*(1), 209–268. (DOI:10.1021/acs.chemrev.1c00553)

[30] Lu J., Pan Q., Zhu S., Liu R., & Zhu H. (2021). Ligand-Mediated Photophysics Adjustability in Bis-tridentate Ir(III) Complexes and Their Application in Efficient Optical Limiting Materials. Inorg Chem, *60*(17), 12835–12846. (DOI:10.1021/acs.inorgchem.1c01142)

[31] Mei J., Leung N. L. C., Kwok R. T. K., Lam J. W. Y., & Tang B. Z. (2015). Aggregation-Induced Emission: Together We Shine, United We Soar! Chem Rev, *115*(21), 11718–11940. (DOI:10.1021/acs.chemrev.5b00263)

[32] Mejía E., Luo S.-P., Karnahl M., Friedrich A., Tschierlei S., Surkus A.-E., Junge H., Gladiali S., Lochbrunner S., & Beller M. (2013). A Noble-Metal-Free System for Photocatalytic Hydrogen Production from Water. Chem Eur J *19*(47), 15972–15978. (DOI:10.1002/chem.201302091)

[33] Mensah A., Shao J.-J., Ni J.-L., Li G.-J., Wang F.-M., & Chen L.-Z. (2022). Recent Progress in Luminescent Cu(I) Halide Complexes: A Mini-Review. Front Chem, *9*. (DOI:10.3389/fchem.2021.816363)

[34] Minozzi C., Caron A., Grenier-Petel J.-C., Santandrea J., & Collins S. K. (2018). Heteroleptic Copper(I)-Based Complexes for Photocatalysis: Combinatorial Assembly, Discovery, and Optimization. Angew Chem Int Ed, *57*(19), 5477–5481. (DOI:10.1002/anie.201800144)

[35] Monti F., Baschieri A., Sambri L., & Armaroli N. (2021). Excited-State Engineering in Heteroleptic Ionic Iridium(III) Complexes. Acc Chem Res, *54*(6), 1492–1505.(DOI:10.1021/acs.accounts.0c00825)

[36] Kinoshita H., & Kano N. (2019). Connecting a carbonyl and a π-conjugated group through a *p* -phenylene linker by (5+1) benzene ring formation. Chem Commun, *55*(59), 8575–8578. (DOI:10.1039/C9CC04012A)

[37] Ni X., Zhang X., Duan X., Zheng H.-L., Xue X.-S., & Ding D. (2019). Near-Infrared Afterglow Luminescent Aggregation-Induced Emission Dots with Ultrahigh Tumor-to-Liver Signal Ratio for Promoted Image-Guided Cancer Surgery. Nano Let*t*, *19*(1), 318–330. (DOI:10.1021/acs.nanolett.8b03936)

[38] Olaru M., Rychagova E., Ketkov S., Shynkarenko Y., Yakunin S., Kovalenko M. V., Yablonskiy A., Andreev B., Kleemiss F., Beckmann J., & Vogt M. (2020). A Small Cationic Organo–Copper Cluster as Thermally Robust Highly Photo- and Electroluminescent Material. J Am Chem Soc, *142*(1), 373–381. (DOI:10.1021/jacs.9b10829)

[39] Peng Q., & Shuai Z. (2021). Molecular mechanism of aggregation-induced emission. *Agg*, *2*(5), e91.(DOI:10.1002/agt2.91)

[40] Prier C. K., Rankic D. A., & MacMillan D. W. C. (2013). Visible Light Photoredox Catalysis with Transition Metal Complexes: Applications in Organic Synthesis. Chem Rev, *113*(7), 5322–5363. (DOI:10.1021/cr300503r)

[41] Sandoval-Pauker C., Santander-Nelli M., & Dreyse P. (2022). Thermally activated delayed fluorescence in luminescent cationic copper(I) complexes. RSC Adv, *12*(17), 10653–10674. (DOI:10.1039/D1RA08082B)

[42] Shen Y., Kong X., Yang F., Bian H.-D., Cheng G., Cook T. R., & Zhang Y. (2022). Deep Blue Phosphorescence from Platinum Complexes Featuring Cyclometalated *N* -Pyridyl Carbazole Ligands with Monocarborane Clusters ($CB_{11}H_{12}^-$). Inorg Chem, *61*(42), 16707–16717. (DOI:10.1021/acs.inorgchem.2c02467)

[43] H., Peng M., Wang J.-J., Feng L.-Z., Yin Y.-C., Song Y.-H., Ru X.-C., Xie Y.-P., Zhang G., Deng Z., & Yao H.-B. (2024). Copper-Iodide Hybrid Clusters with Partial Distortion Enable High-Performance Full-Visible-Spectrum White-Light-Emitting Diodes. *J Am Chem Soc*, *146*(49), 34199–34208. (DOI:10.1021/jacs.4c14545)

[44] Suzuki S., Sasaki S., Sairi A. S., Iwai R., Tang B. Z., & Konishi G. (2020). Principles of Aggregation-Induced Emission: Design of Deactivation Pathways for Advanced AIEgens and Applications. *Angew Chem*, *132*(25), 9940–9951. (DOI:10.1002/ange.202000940)

[45] Tee S. Y., & Ye E. (2021). Recent advancements in coinage metal nanostructures and bio-applications. Mater Adv, *2*(5), 1507–1529. (DOI:10.1039/D0MA00829J)

[46] Troyano J., Zamora F., & Delgado S. (2021). Copper(I)–iodide cluster structures as functional and processable platform materials. Chem Soc Rev, *50*(7), 4606–4628. (DOI:10.1039/D0CS01470B)

[47] Uoyama H., Goushi K., Shizu K., Nomura H., & Adachi C. (2012). Highly efficient organic light-emitting diodes from delayed fluorescence. Nature, *492*(7428), 234–238. (DOI:10.1038/nature11687)

[48] Utrera-Melero R., Mevellec J.-Y., Gautier N., Stephant N., Massuyeau F., & Perruchas S. (2019). Aggregation-Induced Emission Properties of Copper Iodide Clusters. Chem Asian J, *14*(18), 3166–3172. (DOI:10.1002/asia.201900807)

[49] Wang Y., Fang S., Chen X., & Chen S. (2025). Application of photoluminescent materials in cultural relics protection. RSC Adv, *15*(44), 37074–37089. (DOI:10.1039/D5RA05991G)

[50] Wu W., Zhou R., Wang J.-X., Thomas S., Xu Y., Zhu X., Jurado J. P., Yuan X., He T., Hu X., Wang S., Faleiros M. C., Li X., Eddaoudi M., Alshareef H. N., Bakr O. M., & Mohammed O. F. (2025). Unlocking the Core Geometry of High-Efficiency Copper Iodide Cluster Scintillators. J Am Chem Soc, *147*(49), 45452–45461. (DOI:10.1021/jacs.5c15977)

[51] Xu H., Chen R., Sun Q., Lai W., Su Q., Huang W., & Liu X. (2014). Recent progress in metal–organic complexes for optoelectronic applications. Chem. Soc. Rev., *43*(10), 3259–3302. (DOI:10.1039/C3CS60449G)

[52] Yersin, H., Czerwieniec, R., Shafikov, M. Z., & Suleymanova, A. F. (2017). TADF Material Design: Photophysical Background and Case Studies Focusing on CuI and AgI Complexes. Chem Phys Chem, *18*(24), 3508–3535. (DOI:10.1002/cphc.201700872)

[53] Zhang Q., Li N., Wan X., Song X.-F., Zhang Y., Liu H., Miao J., Zou Y., Yang C., & Li K. (2025). Harnessing of Cooperative Cu···H Interactions for Luminescent Low-Coordinate Copper(I) Complexes towards Stable OLEDs. *Angew Chem Int Ed*, *64*(7), e202419290. (DOI:10.1002/anie.202419290)

[54] Zhao Y., Zeng H., Zhu X.-W., Lu W., & Li D. (2021). Metal–organic frameworks as photoluminescent biosensing platforms: Mechanisms and applications. Chem Soc Rev, *50*(7), 4484–4513. (DOI:10.1039/D0CS00955E)

[55] Zhu Y., Deng Y., Li Q., Ding N., Wang Y., Wang M., Zhang K. Y., Liu S., & Zhao Q. (2025). Regulating charge transfer of copper(I) coordination compounds *via* conformation engineering for highly efficient radioluminescence and 3D X-ray imaging. Chem Sci, *16*(47), 22690–22700. (DOI:10.1039/D5SC06329A)

[56] Zobel J. P., Wernbacher A. M., & González L. (2023). Efficient Reverse Intersystem Crossing in Carbene-Copper-Amide TADF Emitters via an Intermediate Triplet State. Angew Chem, *135*(15), e202217620. (DOI:10.1002/ange.202217620)